

# Transition between Supercooled Liquid Water and Ice Crystals in Mixed-phase Clouds based on Airborne In-situ Observations

Flor Vanessa Maciel<sup>1,2</sup>, Minghui Diao<sup>1</sup>, Ching An Yang<sup>1</sup>

<sup>1</sup>Department of Meteorology and Climate Science, San Jose State University, San Jose, 95192, USA

5 <sup>2</sup>*Current affiliation:* Department of Atmospheric and Oceanic Sciences, University of California, Los Angeles, 90095, USA

*Correspondence to:* Minghui Diao (minghui.diao@sjsu.edu)

**Abstract.** The on-set of ice nucleation in mixed-phase clouds determines ice cloud lifetime and their microphysical properties. In this work, we develop a novel method that differentiates various transition phases of mixed-phase clouds, such as clouds dominated by pure liquid or pure ice segments, compared with those having ice crystals surrounded by supercooled liquid water droplets or vice versa. Using this method, we examine the relationship between the macrophysical and microphysical properties of mixed-phase clouds. The results show that the exchange between supercooled liquid water and ice crystals in a macrophysical perspective, represented by the increasing spatial ratio of regions containing ice crystals relative to the total in-cloud region (defined as ice spatial ratio), is positively correlated with the phase exchange in a microphysical perspective, represented by the increasing ice water content (IWC) and decreasing liquid water content (LWC). The mass partition transition from liquid to ice becomes more significant during transition phase 3 when pure ice cloud regions (ICRs) start to appear. Occurrence frequencies of cloud thermodynamic phases show significant transition from liquid to ice at a similar temperature (i.e., -17.5°C) among three types of definitions of mixed-phase clouds based on ice mass fraction, ice number fraction, or ice spatial ratio. Aerosol indirect effects are quantified for different transition phases using number concentrations of aerosols greater than 100 nm or 500 nm ( $N_{>100}$  and  $N_{>500}$ , respectively).  $N_{>500}$  shows stronger positive correlations with ice spatial ratios compared with  $N_{>100}$ . This result indicates that larger aerosols potentially contain ice nucleating particles (INPs), which facilitate the formation of ice crystals in mixed-phase clouds. The impact of  $N_{>500}$  is also more significant in transition phase 2 when ice crystals just start to appear in mixed phase compared with transition phase 3 when pure ICRs have formed, possibly due to the competing aerosol indirect effects on primary and secondary ice production in phase 3. The thermodynamic and dynamic conditions are quantified for each transition phase. The results show in-cloud turbulence as a main mechanism for both the initiation of ice nucleation and the maintenance of supercooled liquid water, while large-scale ascent is important for the latter but not the former. Overall, these results illustrate the varying effects of aerosols, thermodynamics, and dynamics through various stages of mixed-phase cloud evolution based on this new method that categorizes cloud transition phases.

## 1 Introduction

Clouds with different thermodynamic phases can have contrasting influences on the net radiation at the top of atmosphere, depending on their microphysical properties, spatial extent and the distributions of hydrometeors (Matus and L'Ecuyer, 2017). Among three types of cloud phases (i.e., ice, liquid, and mixed), mixed-phase clouds contain both supercooled liquid water and ice crystals. Radiative forcing of mixed-phase clouds over the Southern Ocean has large impacts on Earth's climate based on global climate model simulations (e.g., Tan et al., 2016; Hyder et al., 2018). Evaluating and improving the model parameterizations of mixed-phase clouds requires an improved understanding of their macrophysical and microphysical properties, as well as the factors controlling their formation and evolution.

Previous observations of mixed-phase clouds in the high latitudes have identified complex structures both vertically and horizontally. Using aircraft-based observations over the Southern Ocean, a high frequency of supercooled liquid water was found within low-level clouds in this region, and mixed-phase cloud segments were found to be more spatially heterogeneous compared with the pure liquid and pure ice segments (D'Alessandro et al., 2021). When calculating cloud top phase frequencies as a function of cloud top temperature by using aircraft-based lidar and radar observations over the Southern Ocean, liquid phase was seen as the dominant phase for 74.9% of the cloud top cases with subfreezing temperatures, and supercooled liquid water was found in cloud tops at temperatures as low as  $-30^{\circ}\text{C}$  (Zaremba et al., 2020). Using a large dataset collected by the Convair 580 aircraft of the National Research Council (NRC) of Canada it was found that several microphysical properties are dependent upon temperature, including supercooled liquid droplet concentration (Nliq), IWC, and LWC (Korolev et al., 2003). Ice nucleation within mixed-phase clouds and the factors behind the sustainability of mixed-phase clouds are still topics of contention within the field. The persistent existence of mixed-phase cloud systems has been shown to be affected by local processes such as the formation and growth of cloud droplets and ice crystals (Morrison et al., 2012). The thermodynamics and dynamics of the atmosphere also play a large role in affecting the formation and development of mixed-phase clouds. Using observations of vertical motion within Arctic mixed-phase stratiform, Shupe et al. (2008) showed that an in-cloud updraft sustains the clouds, which also supports growth of ice and liquid mass concentrations. Their results also suggest that ice crystal concentrations (Nice) are often limited in order to support the persistent supercooled liquid water. The connection between ice formation and vertical air velocity at cloud base was examined for mixed-phase clouds with less than 380-m depth by using ground-based Doppler lidar and cloud radar, and the mass flux of IWC was found to increase by two orders of magnitude when the vertical velocity fluctuation increases (Bühl et al., 2019). A study analyzed generating cells of ice crystals inside mixed-phase cloud layers over the Southern Ocean and found that these generating cells have small horizontal widths and contain supercooled liquid water with higher LWC and Nliq than that of the areas between the generating cells, which also held true for ice particles whose dispersions, number concentration, and sizes are larger within the generating cells (Wang et al., 2020). With seven years of ground-based observations at an Alaskan site, it was found that Arctic mixed-phase clouds occur less often in the early fall when the winds are southerly as the atmosphere is more stable, drier, colder and has lower relative humidity. Conversely, during northerly winds they have wider particle distributions (Qiu et al., 2018).

Aerosols have been documented to influence the microphysical properties of mixed-phase clouds around the globe. Field study observations over a fourteen-year time period and from various locations around the Earth were combined to show that both temperature and the number concentration of aerosols larger than 0.5  $\mu\text{m}$  in diameter can impact the concentrations of INPs in mixed-phase clouds (DeMott et al., 2010). From aircraft observations over the Arctic, it was found that entrainment above mixed-phase clouds could enhance Nice and aerosol thermodynamic indirect effect likely occurs (Jackson et al., 2012). Using a nine-year long aerosol dataset, Norgren et al. (2018) found that clean mixed-phase clouds with a lower aerosol loading have higher IWC at their base compared with clouds with a higher aerosol loading. Other studies over the Southern Ocean, e.g., McFarquhar et al. (2021), showed that those environments are primarily pristine, suggesting limited long-range continental aerosol transport and potentially more aerosols newly formed over the high southern latitudes. Observations and simulations of INPs showed that sea spray aerosol may play a major role to initiate primary ice nucleation in low-level mixed-phase clouds over the Southern Ocean (McCluskey et al., 2018). Besides primary ice production, secondary ice production has also been shown to be a critical process enhancing Nice in mixed-phase clouds based on both in-situ airborne observations (Huang et al., 2017; Järvinen et al., 2022) and global climate simulations (Zhao and Liu, 2021; Zhao et al., 2023) over the Southern Ocean. Secondary ice production can also be affected by aerosol loading, e.g., higher concentrations of cloud condensation nuclei can lead to higher supercooled liquid droplet concentrations, and therefore reducing the efficiency of the rime-splintering process.

These aforementioned studies demonstrated that the coexistence and interaction between supercooled liquid droplets and ice crystals hold a key for understanding the persistence of mixed-phase clouds despite of ice–liquid mixtures being unstable. An examination of aerosol indirect effects on liquid and ice hydrometeors separately is also a critical step towards a better understanding of the net aerosol indirect effects on the entire cloud (Korolev et al., 2017; Storelvmo, 2017). Targeting these topics, in this work, we develop a method to identify several transition phases of mixed-phase clouds, by using the spatial relationships among segments containing pure ice or liquid, as well as those containing both ice and liquid. In section 2, a description of the observation dataset and instruments is given. In section 3, the details of the identification of four transition phases, their occurrence frequencies, and comparisons with previously established mixed-phase cloud definitions are provided. A contrast of thermodynamic and dynamic conditions among these transition phases is shown. In addition, the relationships between macrophysical and microphysical properties of mixed-phase clouds during various transition phases are examined. Aerosol indirect effects from larger and smaller aerosols are quantified for individual transition phases. Lastly, in section 4, we discuss the applications of this method for contrasting different definitions of mixed-phase clouds, and the implications of model parameterizations.

**2.1 SOCRATES In-situ Observations and Instrumentation**

The U.S. National Science Foundation (NSF) Southern Ocean Clouds, Radiation, Aerosol Transport Experimental Study (SOCRATES) flight campaign was conducted from January 15<sup>th</sup> to February 24<sup>th</sup> in 2018 (McFarquhar et al., 2021). This NSF-funded campaign utilized the NSF/National Center for Atmospheric Research (NCAR) Gulfstream V (G-V) research aircraft  
95 which flew over the Southern Ocean region of 62°S–42°S and 133°E–164°E as shown in Figure 1. A total of fifteen research flights (RFs) in this campaign were performed with a combined total of 111 flight hours flown. In this work, we applied a temperature restriction of -40°C to 0°C, commonly known as the mixed-phase cloud regime as this temperature range allows for the occurrence of both ice particles and supercooled liquid water, for all our analyses.

The NSF G-V research aircraft during the SOCRATES campaign was equipped with scientific instruments to measure the  
100 various characteristics of the atmosphere, such as aerosol number concentrations (Na), cloud microphysical properties and common meteorological components – temperature, pressure, wind speed and humidity. The temperature was measured by the Rosemount temperature probe. To measure the water vapor molecule number density at 25-Hz resolution the Vertical Cavity Surface Emitting Laser (VCSEL) hygrometer was used. The final data reported the water vapor mixing ratio in 1-Hz resolution and a corrected version of water vapor data based on a post-campaign calibration in summer 2018 is used in this  
105 study (Diao, 2021). The water vapor and temperature data are used to calculate relative humidity with respect to liquid and ice ( $RH_{liq}$  and  $RH_i$ ), by using the equations for saturation vapor pressure with respect to liquid and ice from Murphy and Koop (2005), respectively. The uncertainties associated with  $RH_{liq}$  and  $RH_i$  originate from both water vapor and temperature measurements, which sum up to 6%–7% for the mixed-phase cloud regime. We placed a ceiling on RH values by restricting all  $RH_{liq}$  greater than 101% to 101%. The hydrometeor measurements used in this study were obtained from the Two-  
110 Dimensional Stereo Probe (2DS) and the cloud droplet probe (CDP), which have size ranges at 40 – 5000  $\mu\text{m}$  and 2 – 50  $\mu\text{m}$ , respectively. IWC and LWC are derived from 2DS and CDP probes following the method described in Yang et al. (2021). That is, a mass-Dimension relationship based on a spherical shape is used to calculate LWC for liquid droplets in both CDP and 2DS measurements. A mass-Dimension relationship based on Wu and McFarquhar (2016) is used to calculate IWC for ice particles in 2DS measurements. In-cloud conditions are defined as the 1-Hz measurements with total water content (TWC = IWC+LWC) greater than 0.001  $\text{g m}^{-3}$ . Lower IWC and LWC values have also been reported by the two probes, but the threshold of 0.001  $\text{g m}^{-3}$  is chosen here due to the larger uncertainties of these cloud probes reporting lower mass concentrations of hydrometeors (e.g., Baumgardner et al., 2017). To provide a more focused analysis of cloud layers instead of precipitation below the clouds, we use two remote sensing instruments onboard the G-V aircraft – NSF/NCAR High-performance Instrumented Airborne Platform for Environmental Research (HIAPER) Cloud Radar (HCR) and High Spectral Resolution  
120 Lidar (HSRL) to identify potential precipitating samples. The particle identification (PID) product is used, which includes identifications of 11 categories – rain, supercooled rain, drizzle, supercooled drizzle, cloud liquid, supercooled cloud liquid, melting, large frozen, small frozen, precipitation and cloud (Romatschke and Vivekanandan, 2022). By manually inspecting

hourly time series of this product, we remove segments that are identified as precipitation, supercooled drizzle, drizzle, supercooled rain, and rain. In addition, we further examined the NSF SOCRATES campaign field catalogue for each flight to ensure that we do not miss any precipitation segments that have been identified in the field catalogue. The time stamps of the beginning and end of these segments are stored in supplemental Table S1. For most flights, we identified on average about 5 – 20 minutes of samples of precipitating regions, except RF15 which has about an hour of precipitating samples. It is worth noting that most of these segments occur at temperatures above 0°C, while this study only focuses on -40°C to 0°C.

Aerosol number concentration and size distribution are measured by the Ultra-High Sensitivity Aerosol Spectrometer (UHSAS) which has a size range of 60 – 1000 nanometers (nm). The vertical velocity measurements are derived from several instruments, including Honeywell LASEREF IV Inertial Reference Unit, radome pressure, static pressure, pitot tubes, temperature probe, and differential Global Positioning System, providing an accuracy of  $\sim\pm 0.15\text{--}0.30$  m/s and precision  $\sim 0.01$  m/s (Diao et al., 2015). When examining the in-cloud and clear-sky conditions in the SOCRATES campaign, we noticed a low bias of the original vertical velocity measurements, and therefore applied a correction of +0.125 m/s for the vertical velocity values. After this correction, the peak of the frequency distributions of vertical velocity is centered at 0 m/s for both in-cloud and clear-sky conditions.

## 2.2 Two Previous Datasets for Cloud and Hydrometeor Thermodynamic Phase Classifications

For this work, two previously published datasets regarding thermodynamic phase classifications for the SOCRATES observations are used. Both datasets cover all research flights in the SOCRATES campaign with the exception of research flight 15 due to the malfunction of 2DS probe. The first dataset reports cloud phase (ice, liquid or mixed) at 1-Hz resolution, which was mainly derived from the 2DS and CDP cloud probes (Yang et al., 2021). That method used in Yang et al. (2021) was built upon the study of D’Alessandro et al. (2019) and their figure 1. The cloud phase identification was also verified by other cloud probes, such as the King probe for detecting LWC, and the Rosemount Icing Detector for detecting the existence of supercooled liquid droplets by freezing them when they collide with the detector, which subsequently changes the vibration frequency of the detector. Two modifications are applied to the previous cloud phase identification method of D’Alessandro et al. (2019) and Yang et al. (2021). The first modification is that only when CDP measurements are categorized as liquid droplets, these samples are used in the analysis. Measurements categorized by CDP as ice particles are excluded since previous work has shown that these measurements related to counting ice are most likely artifacts (e.g., Korolev et al., 2013). The second modification is about the treatment of large particles identified as liquid droplets. The previous method restricts particles with maximum dimensions ( $D_{\max}$ )  $> 312.5$   $\mu\text{m}$  as ice particles, while those with  $D_{\max}$  between 112.5 and 312.5  $\mu\text{m}$  can be either liquid or ice depending on the standard deviation of particle sizes measured by 2DS in that second. In this work, we further restrict particles with  $D_{\max} > 212.5$   $\mu\text{m}$  to be ice particles, reducing the number of large particles being categorized as liquid droplets.

The second dataset that detects individual hydrometeor’s thermodynamic phase (either ice or liquid) is also used, which was produced by the University of Washington with the Ice-Liquid Discriminator (UWILD) through a machine learning approach

(Atlas et al., 2021; Mohrmann et al., 2021). Each particle imaged by the 2DS probe is classified particle-by-particle into ice, liquid or unclassified, as 0, 1 and NaN, respectively. In this dataset, the group also provides 1-Hz aggregated data for each research flight that include a quantification of phase-separated particle size distributions (PSDs). We use the hydrometeor count defined by the maximum diameter in the UWILD dataset to calculate Nliq and Nice detected by the 2DS probe within each second. Then we further add Nliq detected by CDP to those detected by 2DS to derive the total Nliq. Finally, we define ice particle number fraction, which equals  $Nice / (Nice + Nliq)$  in one second.

### 3 Results

#### 3.1 A Method to Classify Transition Phases in Mixed-Phase Clouds

A method to classify four transition phases of mixed-phase clouds is developed for 1-Hz aircraft-based observations, which mainly involves two steps. In the first step, three types of cloud segments are identified for each second of observations, including liquid cloud region (LCR), ice cloud region (ICR), and mixed-phase cloud region (MCR). LCR is defined as a 1-Hz in-cloud segment where only supercooled liquid droplets were observed, while ICR is defined as a segment with only ice crystals. MCR is the segment with occurrence of both ice and liquid. Here the identification of liquid and ice at 1-Hz resolution is based on the 1-Hz cloud phase identification method modified from D'Alessandro et al. (2019) and Yang et al. (2021) as described in Section 2.2. In the second step, a total cloud region (TCR) that can potentially contain a combination of LCR, ICR and MCR is identified, which basically is a consecutive in-cloud segment surrounded by clear-sky conditions. If a TCR sample is surrounded by two adjacent seconds of NaN, then this sample is deleted, because one cannot determine if the NaN points are the edge of the cloud or if they are still part of the cloud. But if a TCR sample is surrounded by two adjacent seconds of clear-sky samples, then this in-cloud sample is valid, and its measurement can last from one second to many seconds. For instance, if five seconds of LCR are adjacent to one second of MCR, then both the LCR and MCR belong to the same TCR. An illustration of the identification of TCR is shown in supplemental Figure S1. All the 1-Hz samples within the TCR are used in the analysis in the following sections. The length of each second of sample within an TCR is calculated based on the aircraft true air speed at that specific second. The length of each TCR is calculated as the sum of all in-cloud samples within that TCR. The mean true air speed of the G-V research aircraft between  $-40^{\circ}\text{C}$  and  $0^{\circ}\text{C}$  during the SOCRATES campaign is  $\sim 172$  m/s. Within each TCR, the spatial ratio of LCR, MCR, and ICR relative to TCR is defined as M1, M2 and M3, respectively. Following the calculation of these spatial ratios, four transition phases are defined as follows: (1) only LCR appears in the TCR, (2) MCR coexists with LCR, but no ICR exists, (3) ICR appears and it either resides with LCR, MCR, or both, (4) only ICR appears in the TCR. In other words, phases 1 and 4 stand for pure liquid and ice cloud segments, respectively. Phase 2 represents those ice crystals embedded in MCR and surrounded by supercooled liquid droplets. Phase 3 represents the stage when pockets of pure ice segments start to appear. The four transition phases are depicted in a conceptual diagram in Figure 2. The calculation of M1, M2 and M3 spatial ratios, the definition of each transition phase and their number of samples are summarized in Table 1.

Several potential evolution pathways have been documented and discussed in previous literature, which can be linked with the separation of the four transition phases described above. A “classical” type of evolution pathway follows phases (1) $\Rightarrow$ (2) $\Rightarrow$ (3) $\Rightarrow$ (4), which was observed and documented over 35 years ago (e.g., Hobbs and Rangno, 1985). This type of evolution describes the situation that a cloud is initiated as liquid phase under supercooled conditions; then it experiences ice nucleation and turns into mixed-phase; after that some section of the mixed-phase cloud glaciates and turns into ice; and in the final stage, the entire cloud is glaciated. Besides the classical progression of mixed-phase, there are two other routes of evolution of mixed-phase clouds. The second pathway is when, after nucleation of INPs and turning liquid clouds into mixed-phase, all ice particles precipitate out of the clouds, turning the mixed-phase back into liquid. In other words, the thermodynamic phase evolution of such clouds can be described as liquid  $\Rightarrow$  mixed-phase  $\Rightarrow$  liquid, i.e., phases (1) $\Rightarrow$ (2) $\Rightarrow$ (1). The imbalance between the water vapor supply and the bulk ice mass crystal growth, required for the maintenance of mixed-phase clouds, was discussed in Rauber and Tokay (1991), Pinto (1998), and Westbrook and Illingworth (2011). There is a fair amount of modelling attempts to find an explanation of maintenance of mixed-phase clouds through the balance of INPs and dynamic forcing (e.g., Avramov et al., 2011; Fan et al., 2009, 2011; Smith et al., 2009). The third pathway of mixed-phase evolution is related to the generation of mixed-phase clouds in a pre-existing ice cloud due to dynamic forcing, which can be presented as ice $\Rightarrow$ mixed-phase, i.e., phases (4) $\Rightarrow$ (2), or (4) $\Rightarrow$ (3) $\Rightarrow$ (2). Note that the numerical order of phases 1 – 4 does not necessarily represent the evolution direction. For example, phase 4 may either be the final stage in the first classical pathway, whereas in the third pathway, phase 4 is an initial stage. The theoretical basis explaining such process was developed in several previous studies (e.g., Korolev and Mazin, 2003; Korolev and Field, 2008, Field et al., 2014; Hill et al., 2014). These studies were supported by earlier observations of mixed-phase clouds embedded in pre-existing, deep ice clouds (e.g., Hogan et al., 2002; Field et al., 2004). We caution that a mixed-phase cloud may or may not follow these exact pathways in the real atmosphere, as certain transition phases may be skipped, the evolution direction could be reversed, and multiple phases can appear in the same cloud in a 3-D view. Nevertheless, this method provides a statistical separation of the cloud transition phases and allows a more focused analysis of the coexistence of supercooled liquid water and ice crystals that cannot be achieved solely based on second-by-second measurements (i.e., if one only analyzes seconds with coexisting ice and liquid). Figure 3 a and b show the number of 1-second samples for each transition phase as well as their probability among all transition phases within 5-degree temperature bins. The results show that phases 1 and 4 are more dominant at higher and lower temperatures, respectively, which follows the basic thermodynamic process that the transition from liquid to ice phase occurs more frequently at lower temperatures. At temperatures between -20°C and -5°C, phase 2 is the most dominant phase and contributes to 40% of the total samples, while phase 3 contributes to 20% – 40% of the total samples. The fact that the pure ice or liquid phase only contribute to 5% – 35% of the total samples between -20°C and -5°C demonstrates that the cloud segments sampled in the SOCRATES campaign are spatially heterogeneous, consistent with the results in the previous study of D’Alessandro et al. (2021). Figure 3 c and d show the distributions of the length of TCRs in four phases. The distribution of TCR lengths is consistent with the previously observed power-law distribution of cloud horizontal sizes shown in Wood and Field (2011). Since the 1-D aircraft sampling can be at any vertical level relative to a cloud layer, we further examine the

impacts of restricting the analysis to different ranges of LWC, IWC, and  $RH_i$  values (supplementary Figures S2 – S4). Previous studies such as Wang et al. (2012) and D’Alessandro et al. (2023) have shown that cloud top usually contains higher LWC than cloud base, while IWC increases from the cloud top to cloud base. D’Alessandro et al. (2019) also showed that in-cloud samples with higher liquid mass fraction have higher RH values closer to liquid saturation. By using different ranges of LWC, IWC and  $RH_i$  as proxies for vertical levels within cloud layers, we found that the number of samples of the four transition phases are relatively similar unless very high LWC or IWC are used ( $> 0.1 \text{ g m}^{-3}$ ).

After defining the four transition phases, the following sections will examine both micro- and macrophysical properties of these transition phases, as well as their correlations with each other. Microphysical properties of mixed-phase clouds generally refer to hydrometeor mass concentrations, number concentrations, and size distributions. These microphysical properties can be represented by IWC, LWC,  $N_{ice}$ ,  $N_{liq}$ , and PSDs. On the other hand, macrophysical properties of mixed-phase clouds generally refer to the spatial extent or the spatial fraction of clouds containing supercooled liquid droplets and ice particles. The macrophysical properties can be represented by the lengths of LCR, ICR, MCR, and TCR. In addition, we define two terms – mixed spatial ratio and ice spatial ratio, to represent the spatial fraction of ice-containing clouds in phases 2 and 3, respectively. Specifically, the mixed spatial ratio represents the fraction of MCR as part of an individual, consecutive TCR in phase 2, calculated as length of MCR / length of TCR. Ice spatial ratio represents the fraction of ice-containing segments as part of an individual, consecutive TCR in phase 3, calculated as (length of ICR + length of MCR \* IWC/TWC) / length of TCR. The contribution of MCR to ice spatial ratio in phase 3 is weighted by the ice mass fraction, giving the MCR a smaller weighting function compared with ICR since MCR contains higher fractions of supercooled liquid droplets than ICR. Note that the definitions of mixed spatial ratio and ice spatial ratio differ from the spatial ratio previously used for characterization of mixed-phase clouds in Korolev et al. (2017, Fig.5-13a). In that previous method, the spatial ratio of a certain phase (liquid, mixed or ice) is calculated as the number of samples of that phase divided by the total cloud samples in a certain temperature bin. In this work, the mixed spatial ratio and ice spatial ratio are calculated for individual TCR segments, and therefore each TCR would produce one value for mixed spatial ratio and one value of ice spatial ratio. These values of mixed spatial ratio or ice spatial ratio are applied to every 1-second sample within this TCR.

### 3.2 Thermodynamic and Dynamic Effects on the Evolution of Mixed-phase Clouds

Thermodynamic and dynamic conditions of each transition phase are examined at various temperatures in Figures 4 and 5. Figure 4 shows the entire distributions of  $RH_i$  and standard deviation of vertical velocity ( $\sigma_w$ , calculated for every 40 seconds). Previous theoretical and observational studies (Korolev and Mazin, 2003; Korolev and Isaac, 2006) showed that  $RH_{liq}$  in mixed-phase clouds is close to 100%, due to evaporating droplets rapidly via the Wegner-Bergeron-Findeisen (WBF) process, bringing the system of “droplets-water vapor” to quasi-equilibrium and therefore saturating the environment. As liquid droplets glaciate into ice particles, the peak of RH frequency would also shift towards ice saturation (e.g., D’Alessandro et al., 2019). The in-cloud samples used in this study contain some sub-saturated conditions that deviate from liquid saturation in phases 1 – 3 or from ice saturation in phase 4 (as shown in Figure 4 a – d), which may be attributed to a combination of reasons, such



255 as 6%–7% uncertainties in RH values originated from water vapor and temperature measurement uncertainties, heterogeneous distributions of LCR, MCR and ICR that lead to an uneven distribution of supercooled liquid water, as well as non-equilibrated states between vapor/liquid or vapor/ice phase due to a larger volume being sampled by fast aircraft measurements (~172 m horizontal resolution for 1-Hz measurements used here).

Even though all four phases show some amount of sub-saturation, phase 1 shows the least amount of ice sub-saturated conditions compared with other phases. For all four phases,  $RH_i$  values above ice saturation and closer to liquid saturation  
260 have been seen, providing observational evidence that new formation of supercooled liquid water droplets and ice crystals may occur in any of the four transition phases, following either of the three evolution pathways mentioned in Section 3.1. The variability of  $\sigma_w$  values is slightly larger (0 – 2.5 m/s) in phases 2 and 3, compared with phases 1 and 4 (0 – 1.25 m/s), indicating more turbulent conditions when supercooled liquid water and ice crystals coexist in phases 2 and 3.

265 Figure 5 a – d show the average values of  $RH_{liq}$ ,  $RH_i$ , vertical velocity ( $w$ ) and  $\sigma_w$  at various temperatures, respectively. The number of samples used for Figure 5 is shown in supplemental Figure S5. For the distribution of  $RH_i$  and  $RH_{liq}$ , phase 2 shows the highest RH values, followed by phases 1 and 3. Phase 4 has the lowest  $RH_i$  and  $RH_{liq}$  values. Comparing  $RH_i$  values in regions with and without ice, phase 2 shows higher  $RH_i$  for regions with ice, while phase 3 shows higher  $RH_i$  in regions without ice. This feature can be explained by the fact that higher  $RH_i$  is required in order to initiate ice nucleation in phase 2, while ice  
270 crystals that continue to grow in phase 3 will further reduce  $RH_i$  magnitude by vapor deposition. Based on the analysis in Section 3.3 and Figure 8, the average ice mass fraction (i.e., IWC/TWC) is also lower in phase 2 than phase 3, which suggests that ice crystals in phase 2 would be less effective for relaxing ice supersaturation than those in phase 3.

For distributions of  $w$  in Figure 5 c, phase 1 has slightly higher  $w$  than other phases. Phases 2 – 4 show slightly negative average  $w$  values, suggesting weak downdrafts as the average condition in these phases. For the  $\sigma_w$  distribution (Figure 5 d),  
275 regions with ice in phase 2 have the highest fluctuations of vertical velocity, indicating that stronger in-cloud turbulence induces high  $RH_i$  (as shown in Figure 5 a), which further initiates ice nucleation in phase 2. This result suggests that in-cloud turbulence may be a more prominent mechanism to initiate transition from liquid to ice phase, compared with large-scale uplift (which would be reflected in mean vertical velocity in Figure 5 c if that was the case). Such result is consistent with the finding of Bühl et al. (2019) which showed a positive correlation between IWC mass flux and vertical velocity fluctuation, but this  
280 study further illustrates that in-cloud turbulence is particularly important for transition phase 2 when ice crystals first start to appear inside MCR, surrounded by supercooled liquid water.

The relationship between RH and the spatial expansion of ice-containing regions is examined in Figure 5 e and f. Phase 2 shows nearly constant  $RH_{liq}$  close to liquid saturation when mixed spatial ratio increases (i.e.,  $RH_{liq}$  is within 5% of liquid saturation, which may be caused by combined uncertainties from water vapor and temperature measurements). Differing from  
285 phase 2, phase 3 shows decreasing  $RH_{liq}$  with increasing ice spatial ratio, ranging from 98% to 85%  $RH_{liq}$ . These results indicate that before the appearance of ICR, ice crystals embedded in MCRs do not relax liquid saturation to ice saturation since liquid droplets can still provide additional water vapor by evaporation, e.g., the WBF process. But when ICR starts to appear, RH relaxes to around ice saturation once ice spatial ratio exceeds 0.5. These results are consistent with the previous finding by

290 D'Alessandro et al. (2019) that  $RH_{liq}$  initially is close to liquid saturation with lower ice mass fraction but deviates from liquid saturation as ice mass fraction increases.

The mean values of  $w$  do not vary significantly with mixed spatial ratio or ice spatial ratio (Figure 5 g), but the PDFs of vertical velocity in supplemental Figure S6 b show higher frequencies of updrafts for phases 2 and 3 compared with phases 1 and 4, meaning that the segments containing both supercooled liquid droplets and ice particles are subject to relatively more updrafts, compared with the segments containing only liquid droplets or only ice crystals. This finding is consistent with Shupe et al. (2008) which pointed out the importance of updrafts for sustaining mixed-phase clouds. Differing from the previous studies, our method can further specify that the highest updrafts and vertical velocity fluctuations are found in transition phase 3 when pure ice segments start to appear ( $\sim 4.5$  m/s in Figure S6 b and  $\sim 2.3$  m/s in Figure S6 c), consistent with the fact that  $RH_{liq}$  deviates more from liquid saturation in phase 3 (Figure 5 f), and therefore higher updrafts would be required to maintain supercooled liquid droplets. Analysis of  $\sigma_w$  distribution (Figure 5 h) shows that phase 2 has the highest vertical velocity fluctuations compared with other phases especially at higher mixed spatial ratios, suggesting that even more turbulent condition is needed when supercooled liquid water is surrounded by a large spatial extent of ice-containing regions. Overall, the fact that mean  $w$  values are not significantly different between segments with or without ice in phases 2 and 3 (Figure 5 c) but are more different between phases 2 & 3 versus phases 1 & 4 (Figure S6 b) suggests that higher mean  $w$  is more important for sustaining the supercooled liquid water in coexistence with ice particles than for initiating ice nucleation. These results indicate that both the initiation of ice nucleation and the sustainability of supercooled liquid water are supported by in-cloud turbulence, while large-scale ascent plays an important role in the latter but not the former.

### 3.3 Relationship between Microphysical and Macrophysical Properties of Mixed-phase Clouds

The PSD for four transition phases is shown in Figure 6, separately plotted for the 2DS and CDP probes. Phase 1, 2 and 3 have similar concentrations of small liquid droplets between 2 – 10  $\mu\text{m}$ . Phase 2 has the highest concentrations of hydrometeors at 10 – 60  $\mu\text{m}$ , while phase 3 has the highest concentrations at 60 – 3000  $\mu\text{m}$ . Phase 4 also has relatively high concentrations of ice crystals at 200 – 3000  $\mu\text{m}$ , but they are lower than the values from phase 3 by a factor of 5 – 10. The decreasing ice crystal concentrations per size bin from phase 3 to phase 4 may be caused by stronger aggregation, sublimation, and/or sedimentation of ice crystals in phase 4, as well as by stronger glaciation and/or secondary ice production in phase 3. The significant decrease (1 to 4 orders of magnitude) of hydrometeor concentrations per size bin at 20 – 100  $\mu\text{m}$  in phase 4 compared with the other three phases suggests that most supercooled liquid water may have evaporated and transitioned into ice phase through WBF process or riming, instead of the freezing of individual droplets, while the small ice crystals may have sublimated. It is possible that some of the phase 4 samples may represent the trails of generating cells, where the growth is aloft, and sublimation is at the lower part of the cloud layer. In addition, smaller supercooled liquid droplets require lower temperatures to freeze into ice crystals. This feature is also shown in Figure 6 a – d, as small ice crystals at 20 – 200  $\mu\text{m}$  size range show increasing concentrations with decreasing temperatures. Phase 4 shows a trend of decreasing frequency of large ice particles (e.g.,  $D_{max} > 2000$   $\mu\text{m}$ ) with decreasing temperature. This could be due to an increasing probability of droplet freezing with decreasing

temperature given the same dimension that reduces the available amount of large supercooled liquid droplets for glaciation or riming at lower temperatures. On the other hand, phase 3, which still has supercooled liquid water coexisting with ice particles, does not show such trend, probably because ice crystal growth may occur via various processes in phase 3, such as WBF  
325 process, glaciation, vapor depositional growth under ice supersaturation, and/or riming.

One unique contribution of this work is to quantify how cloud microphysical and macrophysical properties are correlated with each other. The relationship between cloud macrophysical properties (represented by mixed or ice spatial ratio) and several microphysical properties are further examined, including ice particle number fraction (Figure 7), as well as LWC, IWC and ice mass fraction (Figure 8). Linear regressions of the mixed spatial ratio and ice spatial ratio against each microphysical  
330 property are shown for transition phases 2 and 3, respectively. The analysis is separated by LCR, MCR and ICR. The slope value (b) of the linear regression is provided in the text legend. Since transition phase 2 does not contain ICR, no data points are shown in those sub-panels in Figures 7, 8 and 10.

All regions (i.e., LCR, MCR and ICR) in Figure 7 show positive correlations between ice particle number fraction and mixed or ice spatial ratio in phases 2 and 3. This means that while ice crystals gradually dominate the total particle population  
335 (supercooled liquid droplets plus ice particles) in a particular TCR, the segments containing ice particles (i.e., MCR+ICR) also start to dominate the spatial extent of the entire cloud segment (TCR) from a macroscopic perspective. Comparing phase 2 and 3, phase 2 (without ICRs) shows smaller positive correlation (b values of 0.009 and 0.013) compared with phase 3 (b values of 0.561, 0.026, and 0.469). This is because when ice particles are surrounded by supercooled liquid droplets, the latter has a much higher number concentration than ice crystals and therefore ice particle number fractions are relatively low on average  
340 in phase 2. On the other hand, in phase 3, ice crystals start to become the dominant particles by number concentration when ICR appears, and supercooled liquid droplets become less dominant. Similar slope values in Figure 7 b and f indicate that the rates of change of ice particle number fraction in LCR and ICR are similar. That is, as the entire segment TCR becomes more ice dominant, individual LCR and ICR segments embedded inside also experience similar rates of transition from liquid to ice based on number concentrations, except that the ICR has higher ice particle number fraction on average (i.e., higher intercept  
345 values).

Previously, Wang et al. (2020) used airborne remote sensing measurements from the SOCRATES campaign to identify generating cells of ice crystals. Their study showed that inside the generating cells, larger ice particles and higher ice number concentrations were seen, associated with the updrafts inside the cells. These reported generating cells are also analyzed in Figure 7, which shows their average values in each ice spatial ratio bin. The generating cells associated with LCR and MCR  
350 contain lower ice particle number fractions (Figure 7 a – d). But when the generating cells are associated with ice-dominated segments (i.e., ICR), significantly higher ice particle number fractions (close to 1) are seen for most ice spatial ratio bins (Figure 7 f). This result suggests that not all regions within the generating cells experience significant phase transition from liquid to ice, unless the ice-containing regions become dominated by ice.

Figure 8 shows the correlations of LWC and IWC with respect to mixed spatial ratio or ice spatial ratio. A clear negative slope  
355 is seen in Figure 8 a–d, indicating that as the mixed spatial ratio or ice spatial ratio increases, the LWC decreases. On the

contrary, a positive trend is seen in Figure 8 e, f and h, indicating increasing IWC with increasing mixed or ice spatial ratio. These results are consistent with the analysis of ice particle number fraction, showing that the increasing dominance of ice crystals in both mass and number concentrations is correlated with the increasing spatial ratio of ice-containing regions in each TCR. Slope values in Figure 8 illustrate that in phase 2 and 3, LWC decreases more significantly in LCR ( $b = -0.460$ ) than  
360 MCR ( $b = -0.055$ ). Compared with phase 2, phase 3 shows an even stronger decrease of LWC in LCR and MCR with  $b = -1.694$  and  $-0.692$ , respectively. For the changes of IWC, the slope values are similar between MCR and ICR in phase 3 ( $b = 1.358$  and  $1.261$ , respectively), and are slightly lower for MCR in phase 2 ( $b = 0.969$ ). These results indicate that IWC has a similar rate of increase between ice crystals embedded among supercooled liquid droplets (i.e., MCR) and ice crystals in pure ice segments (i.e., ICR) in phases 2 and 3. However, the rate of decrease of LWC with the spatial expansion of ice-containing  
365 regions becomes more significant by a factor of 3 once pure ice segments appear in phase 3 compared with phase 2.

Figure 8 c and j show the positive correlations of ice mass fraction with respect to mixed spatial ratio or ice spatial ratio. Ice mass fraction increases more rapidly with increasing spatial fraction of ice-containing regions in phase 3 than phase 2, with slope values of 1.013 and 0.238, respectively. This result indicates that when ice crystals first appear in MCR, the mass partitioning is still dominated by liquid phase even if ice crystals appear in a high spatial fraction of the cloud segment as part  
370 of MCR. As ice crystals grow into pure ice segments (i.e., ICR), liquid phase starts to rapidly transition into ice phase, suggesting that the formation and growth of ice particles become more significant when pure ice segments appear. This result also indicates that even though ice and supercooled liquid water coexist throughout the lifetime of mixed-phase clouds, the partition between them has different rates of phase change during different transition phases.

To assess the impacts of the sub-saturated conditions within TCR on the main findings of this work, we examine the impacts  
375 of excluding the lower  $RH_i$  samples from the analysis of cloud micro- and macrophysical properties. Supplemental Figures S7 and S8 show the results of excluding  $RH_i < 80\%$  based on the analysis similar to Figures 7 and 8, respectively. The relationships of ice particle number fraction, IWC, LWC and ice mass fractions with respect to mixed spatial ratio and ice spatial ratio show similar results when lower  $RH_i$  are excluded, demonstrating the robustness of these main conclusions.

### 3.4 Comparisons of Three Methods to Define Cloud Thermodynamic Phases

380 The distributions of three cloud thermodynamic phases (ice, liquid, and mixed) are compared between three types of phase identifications, including (i) the 1-Hz cloud phase distribution defined by the ice mass fraction (i.e.,  $IWC/TWC$ ) derived for 1-second observations, i.e., liquid, mixed and ice phases defined as ice mass fraction  $< 0.1$ ,  $0.1 - 0.9$  and  $> 0.9$ , respectively; This method of using ice mass fraction to define mixed-phase clouds has been used in the cloud physics community for approximately thirty years (e.g., Korolev et al., 1998; Korolev et al., 2017, their equation 5-1 and references therein); (ii) cloud  
385 phase distribution defined by the majority of the hydrometeors by particle number concentrations using the combined CDP and 2DS data, i.e., liquid (ice) phase defined as a second of data with more than 90% (less than 10%) of hydrometeor particle number concentrations being liquid droplets, and mixed phase defined as a second of data with 10% – 90% of particle number concentrations being liquid droplets; (iii) cloud phases defined by the ice spatial ratio within each TCR using the method

developed in this work. Liquid, mixed, and ice phases are defined as where the ice spatial ratio of an entire TCR is  $< 0.1$ ,  $0.1$   
390  $- 0.9$  and  $> 0.9$ , respectively. To summarize, each of these three types of methods relies on a certain type of fraction of ice  
crystals relative to the total hydrometeors, either in terms of 1-Hz mass fraction, 1-Hz particle number fraction, or in terms of  
the spatial fraction relative to the entire cloud segment. This concept of using various ice fractions to define cloud  
thermodynamic phases has been summarized in the previous review article by Korolev et al. (2017).  
Figure 9 shows the occurrence frequencies of cloud thermodynamic phases in relation to temperature compared among three  
395 identification methods. The results show that all three methods have similar distributions of three thermodynamic phases at  
temperatures above  $-30^{\circ}\text{C}$ . For the lowest temperature bins close to  $-40^{\circ}\text{C}$ , the particle-by-particle identification may have  
difficulties discerning single hydrometeors as frozen droplets, supercooled liquid droplets or small ice crystals, which leads to  
the large increase in mixed phase frequency in that bin. For temperatures between  $-20^{\circ}\text{C}$  and  $0^{\circ}\text{C}$ , the ice spatial ratio method  
has slightly higher mixed phase frequency ( $0.1 - 0.2$ ) than the ice particle number fraction method ( $\sim 0.1$ ). The ice mass fraction  
400 method has the lowest mixed phase frequency among all three methods, at  $0.03 - 0.07$ . Overall, all three methods show a  
significant transition from liquid to ice phase at a similar temperature around  $-17.5^{\circ}\text{C}$ . This indicates that the major transition  
from liquid to ice is reflected in both cloud microphysical (i.e., mass partition and number partition) and macrophysical  
properties (spatial extent partition). The rapid increase of occurrence of ice clouds in the temperature range of  $-15^{\circ}\text{C}$  to  $-20^{\circ}\text{C}$   
was also observed by previous studies (e.g., Wallace and Hobbs, 1977; Moss and Johnson, 1994). The analysis of Figure 9 is  
405 also conducted for only  $\text{RH}_i > 80\%$  in supplementary Figure S9 and the results show consistent results of the cloud phase  
frequency distributions regardless of the exclusion of low  $\text{RH}_i$  values.

### 3.5 Aerosol Indirect Effects on the Evolution of Mixed-phase Clouds

The relationship between aerosol number concentration and mixed spatial ratio or ice spatial ratio is examined in Figure 10.  
Due to the possible complication of in-cloud measurements of aerosol number concentrations, we applied a moving average  
410 to calculate logarithmic scales of aerosol concentrations at every 50 seconds in Figure 10. A coarser spatial averaging using  
the 100-second moving average is also shown in supplementary Figure S10.

Number concentrations of larger aerosols (diameters  $> 500$  nm, namely  $N_{>500}$ ) and smaller aerosols (diameters  $> 100$  nm,  
namely  $N_{>100}$ ) are analyzed in Figure 10 a – h and i – p, respectively. The slope values of the linear regressions show strong  
positive correlations between  $N_{>500}$  and ice spatial ratio in phase 2 (Figure 10 g,  $b = 1.198$ ), when ice crystals just start to  
415 appear and are surrounded by supercooled liquid droplets. Such positive correlation becomes weaker in phase 3 (Figure 10 h,  
 $b = 0.721$ ), when ICR starts to appear. The stronger positive correlation with  $N_{>500}$  in phase 2 is likely due to primary ice  
nucleation (such as heterogeneous nucleation) playing a major role in phase 2 when ice crystals first start to appear. On the  
other hand, secondary ice production may occur more frequently in phase 3, and secondary ice production via rime-splintering  
is less effective when concentrations of cloud condensation nuclei are higher. For the correlations with  $N_{>100}$ , a positive trend  
420 is still seen with respect to ice spatial ratio in MCR and ICR, indicating possible pathways of ice formation via condensation  
freezing and immersion freezing assisted by smaller aerosols. Overall, the weaker positive correlations with  $N_{>100}$  in MCR and

ICR compared with  $N_{>500}$  indicates that larger aerosols play a more dominant role for initiating ice nucleation than smaller aerosols. Stronger positive correlations between IWC and  $N_{>500}$  compared with  $N_{>100}$  are also shown in the previous work by Yang et al. (2021), although that study did not differentiate the transition phase of clouds nor examine aerosol indirect effects in relation to cloud macrophysical properties, i.e., the spatial expansion of ice-containing cloud segments.

#### 4 Discussion and Conclusions

Mixed-phase clouds are ubiquitous in the atmosphere and in order to fully capture their extent of impacts on Earth's climate, more studies need to be conducted in order to investigate their formation, evolution, and aerosol effects on their microphysical and macrophysical characteristics. Therefore, in this study, a novel method that categorizes mixed-phase clouds into four transition phases was presented. This method allows an investigation on the evolution of cloud macrophysical and microphysical properties, as well as the related aerosol indirect effects, as the phase change occurs among vapor, liquid, and solid phase of water molecules.

The relationships between microphysical and macrophysical properties are examined, which addresses the question of whether the dominance of ice crystals in hydrometeor mass or number concentration also leads to the dominance of ice-containing regions in a consecutive in-cloud segment. Two spatial extent parameters – mixed spatial ratio and ice spatial ratio – are used to identify the spatial transition between supercooled liquid water-dominant and ice-dominant mixed phase clouds. Positive correlations of ice particle number fraction and IWC in relation to mixed spatial ratio and ice spatial ratio are seen in both transition phases 2 and 3, respectively. Comparing phases 2 and 3, the latter phase shows higher rates of changes in all three microphysical properties with increasing ice spatial ratio, including faster increase of ice number fraction, faster increase of IWC, and faster decrease of LWC. These results indicate that when ice crystals become more dominant and pure ice segments start to appear, both the mass and number partitions between liquid phase and ice phase experience a higher rate of transition. The correlations between various cloud macro- and microphysical properties are further demonstrated by using three methods to define ice, liquid, and mixed phases. Following the generic definition of mixed-phase clouds described in Korolev et al. (1998) and Korolev et al. (2017),  $\mu_{ice} = \alpha_{ice} / (\alpha_{ice} + \alpha_{liq})$ , where  $\mu_{ice}$  is ice phase fraction, and  $\alpha_{ice}$  and  $\alpha_{liq}$  are specific cloud microphysical properties. We examined  $\alpha_{ice}$  being ice mass fraction or ice particle number fraction at 1-Hz resolution, but also extended the definition to include  $\alpha_{ice}$  being ice spatial ratio in a consecutive cloud segment, which is a macrophysical property that has not been investigated before. All three methods follow the same thresholds of  $< 0.1$ ,  $0.1 - 0.9$ , and  $> 0.9$  to separate  $\mu_{ice}$  into liquid, mixed and ice phases, respectively. As a result, all three methods identify a significant transition from liquid to ice around a similar temperature at  $-17.5^\circ\text{C}$ . A minor difference among three methods is that mixed-phase cloud frequency between  $-20^\circ\text{C}$  to  $0^\circ\text{C}$  is slightly higher when defined by ice number fraction and ice spatial ratio ( $0.1 - 0.2$ ) compared with that defined by ice mass fraction ( $0.05$ ). Such comparison on various phase definition methods indicates that a spatial extent-based cloud phase identification method, such as using number of pixels in remote sensing data by Yip et al. (2021) and Desai et al. (2023), can produce similar statistical distributions of liquid and ice phases compared with other methods based on ice

mass fraction, e.g., D'Alessandro et al. (2019) and Yang et al. (2021), while the spatial extent-based method produces a slightly  
455 higher mixed-phase cloud frequency. Future analysis of cloud phase distributions based on different types of observation  
techniques and model simulations is recommended to consider this comparison result, especially when evaluating model output  
against observations using different definitions of mixed-phase clouds.

Differing from previous studies on the coexistence of ice crystals and supercooled liquid water, the method presented in this  
work allows one to separately examine the cases when ice crystals are surrounded by supercooled liquid water in MCR (phase  
460 2) and compare them with cases when ice crystals become more dominant in ICR (phase 3). Because of this, aerosol indirect  
effects on various stages of clouds can also be examined separately. Number concentrations of aerosols larger than 500 nm  
show stronger positive correlations with mixed spatial ratio and ice spatial ratio compared with aerosols larger than 100 nm.  
This indicates that the larger aerosols are more likely to act as INPs to initiate primary ice nucleation. Transition phase 3 shows  
a slightly weaker positive correlation of ice spatial ratio with aerosol number concentrations (i.e.,  $N_{>500}$  and  $N_{>100}$ ) compared  
465 with phase 2, indicating that the aerosol indirect effects are more prominent when ice crystals first start to appear amongst  
supercooled liquid water in MCR. Such weaker aerosol indirect effects in phase 3 are possibly due to a competition between  
the positive correlation of primary ice nucleation with aerosol number concentrations and the negative correlation of secondary  
ice production with aerosol number concentrations. When pure ice segments (ICR) start to appear, it is possible that secondary  
ice production plays a more important role and therefore the net aerosol indirect effects become weaker.

470 Thermodynamic and dynamic conditions are examined for each transition phase, especially for two key stages of mixed-phase  
clouds – the initiation of ice nucleation in MCR and the coexistence of liquid and ice after pure ice segments are formed. The  
results show that regions with ice crystals in phase 2 are associated with the highest  $RH_i$  values as well as the highest fluctuation  
of vertical velocity. This result indicates that in-cloud turbulence is likely the main mechanism to produce higher  $RH_i$  in order  
to initiate ice nucleation. Averages of vertical velocity do not show significantly higher values for phase 2, indicating the large-  
475 scale ascent plays a less important role for initiating the transition from liquid to ice compared with in-cloud turbulence in the  
SOCRATES campaign. As for the dynamical conditions supporting the coexistence of liquid and ice, previously, several  
dynamic mechanisms were proposed in the study of Korolev and Field (2008), highlighting the critical thresholds of vertical  
motion for sustaining supercooled liquid water. Our analysis shows that both ascent and in-cloud turbulence are more  
frequently observed in segments containing both ice and liquid (i.e., phases 2 and 3 versus phases 1 and 4 shown in  
480 supplementary Figure S6 b), indicating that higher updrafts are needed to sustain supercooled liquid water when they are  
surrounded by ice crystals. This observation-based method can be used to assess the contribution from different dynamic  
mechanisms for maintaining different evolution stages of mixed-phase clouds in various field campaigns.

The definition of LCR, MCR and ICR is also related to the two types of mixed-phase clouds – genuinely versus conditionally  
mixed, separated by the level of mixing between supercooled liquid water and ice crystals (e.g., Korolev et al., 2017, their Fig.  
485 5-1; Korolev and Milbrandt, 2022, their Fig. 1). The scenario of “LCR+ICR” identified as one sub-category of phase 3 would  
be considered a conditionally mixed-phase cloud, which may form a sequence of spatially adjacent cloud segments ...-ice-  
liquid-ice-liquid-.... Such clouds may be thermodynamically stable, and their lifetime would be determined by processes other

than the interaction between ice and liquid (e.g., WBF and riming). This special scenario when only “LCR+ICR” exist in the TCR without the existence of MCR has 840 seconds of samples, which is a small fraction of the total 11988 seconds of transition phase 3 samples. This result suggests that most of the clouds with coexisting supercooled liquid water and ice particles at least contain some partial segments as genuinely mixed phase, i.e., MCR.

Parameterizations of mixed-phase clouds in climate models often rely on a tunable parameter that can modify the mixing volume between ice and liquid (e.g., Tan and Storelvmo, 2016; Zhang et al., 2019). In other words, if ice crystals are mixed uniformly amongst supercooled liquid water within a model grid box, the WBF process would become more effective and the transition from liquid to ice would be faster. This study illustrates that the rates of phase change are strongly affected by the existence of pure ice segments, not only by the mixed spatial ratio or ice spatial ratio which reflects how extensive the spatial coverage of ice crystals is (Figure 8). Future model parameterization development is recommended to consider the varying rates of phase change due to the spatial and temporal variabilities of how liquid and ice spatially overlap with each other throughout a cloud’s lifetime.

Overall, the method proposed in this work provides a unique perspective to assess various evolution stages of mixed phase clouds, especially the transition from liquid to ice phase. Such transition can be reflected in particle number fraction, mass fraction, and spatial ratio. We note that this is an idealized method with its own caveats. For example, the evolution of mixed-phase clouds may not always follow a simple direction from phase 1 to 4. In addition, the aircraft observations used here only capture the 1-D structure of a cloud segment, while cloud layers above and below the aircraft flight track may show a different ice spatial ratio on a 2-D or 3-D view. Nevertheless, this method helps to provide a statistical categorization of different transition phases of mixed-phase clouds solely based on Eulerian-view sampling of aircraft data, which enables more detailed examination from a statistical, quasi-Lagrangian view that was not available previously. Future investigation that compares 1-D aircraft sampling with 2-D remote sensing observations and 3-D model simulations is recommended to further examine the quasi-Lagrangian evolution of mixed-phase clouds.

## 510 **Data availability**

Observations from the NSF SOCRATES campaign are accessible at <https://data.eol.ucar.edu/>.

## **Author contributions**

F. Maciel, M. Diao, and C.A. Yang contributed to the development of the ideas, conducted quality control to aircraft-based observations, and conducted data analysis. F. Maciel and M. Diao wrote the manuscript.



## 515 **Competing interests**

The authors declare that they have no conflict of interest.

## **Acknowledgments**

F. Maciel, C.A. Yang and M. Diao acknowledge funding from NSF OPP #1744965. M. Diao acknowledges the funding support from U.S. Department of Energy (DOE) Atmospheric System Research (ASR) grant DE-SC0021211 and RDPP grant DE-520 SC0023155. C.A. Yang and M. Diao acknowledge funding from SJSU Division of Research and Innovation award number 22-LUG-08-006. F. Maciel and C.A. Yang also acknowledges support from the San Jose State University Walker Fellowship.

## **References**

- Atlas, R., Mohrmann, J., Finlon, J., Lu, J., Hsiao, I., Wood, R., and Diao, M.: The University of Washington Ice–Liquid Discriminator (UWILD) improves single-particle phase classifications of hydrometeors within Southern Ocean clouds using machine learning, *Atmos. Meas. Tech.*, 14, 7079–7101, <https://doi.org/10.5194/amt-14-7079-2021>, 2021.
- Avramov, A., Ackerman, A. S., Fridlind, A. M., Van Diedenhoven, B., Botta, G., Aydin, K., Verlinde, J., Korolev, A. V., Strapp, J. W., McFarquhar, G. M., Jackson, R., Brooks, S. D., Glen, A., and Wolde, M.: Toward ice formation closure in Arctic mixed-phase boundary layer clouds during ISDAC, *J. Geophys. Res. Atmos.*, 116, 0–08, <https://doi.org/10.1029/2011JD015910>, 2011.
- 530 Baumgardner, D., Abel, S. J., Axisa, D., Cotton, R., Crosier, J., Field, P., Gurganus, C., Heymsfield, A., Korolev, A., Krämer, M., Lawson, P., McFarquhar, G., Ulanowski, Z., and Um, J.: Cloud Ice Properties: In Situ Measurement Challenges, *Meteorol. Monogr.*, 58, 9.1-9.23, <https://doi.org/10.1175/AMSMONOGRAPHS-D-16-0011.1>, 2017.
- Bühl, J., Seifert, P., Engelmann, R., and Ansmann, A.: Impact of vertical air motions on ice formation rate in mixed-phase cloud layers, *npj Clim. Atmos. Sci.*, 2, 36, <https://doi.org/10.1038/s41612-019-0092-6>, 2019.
- 535 D’Alessandro, J. J., Diao, M., Wu, C., Liu, X., Jensen, J. B., and Stephens, B. B.: Cloud phase and relative humidity distributions over the Southern Ocean in austral summer based on in situ observations and CAM5 simulations, *J. Clim.*, 32, 2781–2805, <https://doi.org/10.1175/JCLI-D-18-0232.1>, 2019.
- D’Alessandro, J. J., McFarquhar, G. M., Wu, W., Stith, J. L., Jensen, J. B., and Rauber, R. M.: Characterizing the Occurrence and Spatial Heterogeneity of Liquid, Ice, and Mixed Phase Low-Level Clouds Over the Southern Ocean Using in Situ Observations Acquired During SOCRATES, *J. Geophys. Res. Atmos.*, 126, 1–18, <https://doi.org/10.1029/2020JD034482>, 2021.
- 540 D’Alessandro, J. J., McFarquhar, G. M., Stith, J. L., Diao, M., DeMott, P. J., McCluskey, C. S., et al.: An evaluation of phase, aerosol-cloud interactions and microphysical properties of single- and multi-layer clouds over the Southern Ocean using in

- situ observations from SOCRATES. *Journal of Geophysical Research: Atmospheres*, 128, e2023JD038610.   
545 <https://doi.org/10.1029/2023JD038610>, 2023.
- DeMott, P. J., Prenni, A. J., Liu, X., Kreidenweis, S. M., Petters, M. D., Twohy, C. H., Richardson, M. S., Eidhammer, T., and Rogers, D. C.: Predicting global atmospheric ice nuclei distributions and their impacts on climate, *Proc. Natl. Acad. Sci.*, 107, 11217–11222, <https://doi.org/10.1073/pnas.0910818107>, 2010.
- Desai, N., Diao, M., Shi, Y., Liu, X., and Silber, I.: Ship-based observations and climate model simulations of cloud phase   
550 over the Southern Ocean. *Journal of Geophysical Research: Atmospheres*, 128, e2023JD038581. <https://doi.org/10.1029/2023JD038581>, 2023.
- Diao, M., Jensen, J. B., Pan, L. L., Homeyer, C. R., Honomichl, S., Bresch, J. F., and Bansemer, A.: Distributions of ice supersaturation and ice crystals from airborne observations in relation to upper tropospheric dynamical boundaries. *J. Geophys. Res. Atmos.*, 120, 5101–5121. doi: 10.1002/2015JD023139, 2015.
- 555 Diao, M.: VCSEL 1Hz Water Vapor Data, <https://doi.org/10.26023/KFSD-Y8DQ-YC0D>, 2021.
- Fan, J., Ovtchinnikov, M., Comstock, J. M., McFarlane, S. A., and Khain, A.: Ice formation in Arctic mixed-phase clouds: Insights from a 3-D cloud-resolving model with size-resolved aerosol and cloud microphysics, *J. Geophys. Res.*, 114, <https://doi.org/10.1029/2008JD010782>, 2009.
- Fan, J., Ghan, S., Ovchinnikov, M., Liu, X., Rasch, P. J., and Korolev, A.: Representation of Arctic mixed-phase clouds and   
560 the Wegener-Bergeron-Findeisen process in climate models: Perspectives from a cloud-resolving study, *J. Geophys. Res. Atmos.*, 116, <https://doi.org/10.1029/2010JD015375>, 2011.
- Field, P. R., Hogan, R. J., Brown, P. R. A., Illingworth, A. J., Choulaton, T. W., Kaye, P. H., Hirst, E., and Greenaway, R.: Simultaneous radar and aircraft observations of mixed-phase cloud at the 100 m scale, *Q. J. R. Meteorol. Soc.*, 130, 1877–1904, <https://doi.org/10.1256/QJ.03.102>, 2004.
- 565 Field, P. R., Hill, A. A., Furtado, K., and Korolev, A.: Mixed-phase clouds in a turbulent environment. Part 2: Analytic treatment, *Q. J. R. Meteorol. Soc.*, 140, 870–880, <https://doi.org/10.1002/QJ.2175>, 2014.
- Hill, A. A., Field, P. R., Furtado, K., Korolev, A., and Shipway, B. J.: Mixed-phase clouds in a turbulent environment. Part 1: Large-eddy simulation experiments, *Q. J. R. Meteorol. Soc.*, 140, 855–869, <https://doi.org/10.1002/QJ.2177>, 2014.
- Hobbs, P. V. and Rangno, A. L.: Ice Particle Concentrations in Clouds, *J. Atmos. Sci.*, 42, 2523–2549,   
570 [https://doi.org/10.1175/1520-0469\(1985\)042<2523:IPCIC>2.0.CO;2](https://doi.org/10.1175/1520-0469(1985)042<2523:IPCIC>2.0.CO;2), 1985.
- Hogan, R. J., Field, P. R., Illingworth, A. J., Cotton, R. J., and Choulaton, T. W.: Properties of embedded convection in warm-frontal mixed-phase cloud from aircraft and polarimetric radar, *Q. J. R. Meteorol. Soc.*, 128, 451–476, <https://doi.org/10.1256/003590002321042054>, 2002.
- Huang, Y., Chubb, T., Baumgardner, D., DeHoog, M., Siems, S. T., and Manton, M. J.: Evidence for secondary ice production   
575 in Southern Ocean open cellular convection, *Q. J. R. Meteorol. Soc.*, 143, 1685–1703, <https://doi.org/10.1002/qj.3041>, 2017.
- Hyder, P., Edwards, J. M., Allan, R. P., Hewitt, H. T., Bracegirdle, T. J., Gregory, J. M., Wood, R. A., Meijers, A. J. S., Mulcahy, J., Field, P., Furtado, K., Bodas-Salcedo, A., Williams, K. D., Copsey, D., Josey, S. A., Liu, C., Roberts, C. D.,

- Sanchez, C., Ridley, J., Thorpe, L., Hardiman, S. C., Mayer, M., Berry, D. I., and Belcher, S. E.: Critical Southern Ocean climate model biases traced to atmospheric model cloud errors, *Nat. Commun.*, 9, 3625, <https://doi.org/10.1038/s41467-018-05634-2>, 2018.
- Jackson, R. C., McFarquhar, G. M., Korolev, A. V., Earle, M. E., Liu, P. S. K., Lawson, R. P., Brooks, S., Wolde, M., Laskin, A., and Freer, M.: The dependence of ice microphysics on aerosol concentration in arctic mixed-phase stratus clouds during ISDAC and M-PACE, *J. Geophys. Res. Atmos.*, 117, 1–20, <https://doi.org/10.1029/2012JD017668>, 2012.
- Järvinen, E., McCluskey, C. S., Waitz, F., Schnaiter, M., Bansemmer, A., Bardeen, C. G., Gettelman, A., Heymsfield, A., Stith, J. L., Wu, W., D'Alessandro, J. J., McFarquhar, G. M., Diao, M., Finlon, J. A., Hill, T. C. J., Levin, E. J. T., Moore, K. A., and DeMott, P. J.: Evidence for Secondary Ice Production in Southern Ocean Maritime Boundary Layer Clouds, *J. Geophys. Res. Atmos.*, 127, 1–31, <https://doi.org/10.1029/2021JD036411>, 2022.
- Korolev, A. V., Strapp, J. W., Isaac, G. A., and Nevzorov, A. N.: The Nevzorov Airborne Hot-Wire LWC–TWC Probe: Principle of Operation and Performance Characteristics, *J. Atmos. Ocean. Technol.*, 15, 1495–1510, [https://doi.org/10.1175/1520-0426\(1998\)015<1495:TNAHWL>2.0.CO;2](https://doi.org/10.1175/1520-0426(1998)015<1495:TNAHWL>2.0.CO;2), 1998.
- Korolev, A. V., Isaac, G. A., Cober, S. G., Strapp, J. W., and Hallett, J.: Microphysical characterization of mixed-phase clouds, *Q. J. R. Meteorol. Soc.*, 129, 39–65, <https://doi.org/10.1256/qj.01.204>, 2003.
- Korolev, A. V. and Mazin, I. P.: Supersaturation of water vapor in clouds, *J. Atmos. Sci.*, 60, 2957–2974, [https://doi.org/10.1175/1520-0469\(2003\)060<2957:SOWVIC>2.0.CO;2](https://doi.org/10.1175/1520-0469(2003)060<2957:SOWVIC>2.0.CO;2), 2003.
- Korolev, A. V. and Isaac, G. A.: Relative Humidity in Liquid, Mixed-Phase, and Ice Clouds, *J. Atmos. Sci.*, 63, 2865–2880, <https://doi.org/10.1175/JAS3784.1>, 2006.
- Korolev, A. V. and Field, P. R.: The Effect of Dynamics on Mixed-Phase Clouds: Theoretical Considerations, *J. Atmos. Sci.*, 65, 66–86, <https://doi.org/10.1175/2007JAS2355.1>, 2008.
- Korolev, A. V., Emery, E. F., Strapp, J. W., Cober, S. G., and Isaac, G. A.: Quantification of the effects of shattering on airborne ice particle measurements, *J. Atmos. Ocean. Technol.*, 30, 2527–2553, <https://doi.org/10.1175/JTECH-D-13-00115.1>, 2013.
- Korolev, A. V., McFarquhar, G., Field, P. R., Franklin, C., Lawson, P., Wang, Z., Williams, E., Abel, S. J., Axisa, D., Borrmann, S., Crosier, J., Fugal, J., Krämer, M., Lohmann, U., Schlenzcek, O., Schnaiter, M., and Wendisch, M.: Mixed-Phase Clouds: Progress and Challenges, *Meteorol. Monogr.*, 58, 5.1-5.50, <https://doi.org/10.1175/AMSMONOGRAPHS-D-17-0001.1>, 2017.
- Korolev, A. V. and Milbrandt, J.: How Are Mixed-Phase Clouds Mixed?, *Geophys. Res. Lett.*, 49, 1–7, <https://doi.org/10.1029/2022GL099578>, 2022.
- Matus, A. V and L'Ecuyer, T. S.: The role of cloud phase in Earth's radiation budget, *J. Geophys. Res. Atmos.*, 122, 2559–2578, <https://doi.org/10.1002/2016JD025951>, 2017.
- McCluskey, C. S., Hill, T. C. J., Humphries, R. S., Rauker, A. M., Moreau, S., Stratton, P. G., Chambers, S. D., Williams, A. G., McRobert, I., Ward, J., Keywood, M. D., Harnwell, J., Ponsonby, W., Loh, Z. M., Krummel, P. B., Protat, A., Kreidenweis,

- S. M., and DeMott, P. J.: Observations of Ice Nucleating Particles Over Southern Ocean Waters, *Geophys. Res. Lett.*, 45, 11,989–11,997, <https://doi.org/10.1029/2018GL079981>, 2018.
- McFarquhar, G. M., Bretherton, C. S., Marchand, R., Protat, A., DeMott, P. J., Alexander, S. P., Roberts, G. C., Twohy, C.  
615 H., Toohey, D., Siems, S., Huang, Y., Wood, R., Rauber, R. M., Lasher-Trapp, S., Jensen, J., Stith, J. L., Mace, J., Um, J.,  
Järvinen, E., Schnaiter, M., Gettelman, A., Sanchez, K. J., McCluskey, C. S., Russell, L. M., McCoy, I. L., Atlas, R. L.,  
Bardeen, C. G., Moore, K. A., Hill, T. C. J., Humphries, R. S., Keywood, M. D., Ristovski, Z., Cravigan, L., Schofield, R.,  
Fairall, C., Mallet, M. D., Kreidenweis, S. M., Rainwater, B., D'Alessandro, J., Wang, Y., Wu, W., Saliba, G., Levin, E. J. T.,  
Ding, S., Lang, F., Truong, S. C. H., Wolff, C., Haggerty, J., Harvey, M. J., Klekociuk, A. R., and McDonald, A.: Observations  
620 of Clouds, Aerosols, Precipitation, and Surface Radiation over the Southern Ocean: An Overview of CAPRICORN, MARCUS,  
MICRE, and SOCRATES, *Bull. Am. Meteorol. Soc.*, 102, E894–E928, <https://doi.org/10.1175/BAMS-D-20-0132.1>, 2021.
- Mohrmann, J., et al. 2021. University of Washington Ice-Liquid Discriminator single particle phase classifications and 1 Hz  
particle size distributions/heterogeneity estimate. Version 1.0. UCAR/NCAR— Earth Observing Laboratory.  
<https://doi.org/10.26023/PA5W-4DRX-W50A>. Accessed 21 Aug 2022.
- 625 Morrison, H., de Boer, G., Feingold, G., Harrington, J., Shupe, M. D., and Sulia, K.: Resilience of persistent Arctic mixed-  
phase clouds, *Nat. Geosci.*, 5, 11–17, <https://doi.org/10.1038/ngeo1332>, 2012.
- Moss, S. J. and Johnson, D. W.: Aircraft measurements to validate and improve numerical model parametrisations of ice to  
water ratios in clouds, *Atmos. Res.*, 34, 1–25, [https://doi.org/10.1016/0169-8095\(94\)90078-7](https://doi.org/10.1016/0169-8095(94)90078-7), 1994.
- Murphy, D. M. and Koop, T.: Review of the vapour pressures of ice and supercooled water for atmospheric applications, *Q.*  
630 *J. R. Meteorol. Soc.*, 131, 1539–1565, <https://doi.org/10.1256/qj.04.94>, 2005.
- Norgren, M. S., de Boer, G., and Shupe, M. D.: Observed aerosol suppression of cloud ice in low-level Arctic mixed-phase  
clouds, *Atmos. Chem. Phys.*, 18, 13345–13361, <https://doi.org/10.5194/acp-18-13345-2018>, 2018.
- Pinto, J. O.: Autumnal mixed-phase cloudy boundary layers in the arctic, *J. Atmos. Sci.*, 55, 2016–2038,  
[https://doi.org/10.1175/1520-0469\(1998\)055<2016:AMPCBL>2.0.CO;2](https://doi.org/10.1175/1520-0469(1998)055<2016:AMPCBL>2.0.CO;2), 1998.
- 635 Qiu, S., Xi, B., and Dong, X.: Influence of Wind Direction on Thermodynamic Properties and Arctic Mixed-Phase Clouds in  
Autumn at Utqiagvik, Alaska, *J. Geophys. Res. Atmos.*, 123, 9589–9603, <https://doi.org/10.1029/2018JD028631>, 2018.
- Rauber, R. M. and Tokay, A.: An Explanation for the Existence of Supercooled Water at the Top of Cold Clouds, *J. Atmos.*  
*Sci.*, 48, 1005–1023, [https://doi.org/10.1175/1520-0469\(1991\)048<1005:AEFTEO>2.0.CO;2](https://doi.org/10.1175/1520-0469(1991)048<1005:AEFTEO>2.0.CO;2), 1991.
- Romatschke, U., and Vivekanandan, J.: Cloud and precipitation particle identification using cloud radar and lidar  
640 measurements: Retrieval technique and validation. *Earth and Space Science*, 9, e2022EA002299.  
<https://doi.org/10.1029/2022EA002299>, 2022.
- Shupe, M. D., Kollias, P., Persson, P. O. G., and McFarquhar, G. M.: Vertical Motions in Arctic Mixed-Phase Stratiform  
Clouds, *J. Atmos. Sci.*, 65, 1304–1322, <https://doi.org/10.1175/2007JAS2479.1>, 2008.
- Smith, A. J., Larson, V. E., Niu, J., Kankiewicz, J. A., and Carey, L. D.: Processes that generate and deplete liquid water and  
645 snow in thin midlevel mixed-phase clouds, *J. Geophys. Res. Atmos.*, 114, 1–18, <https://doi.org/10.1029/2008JD011531>, 2009.

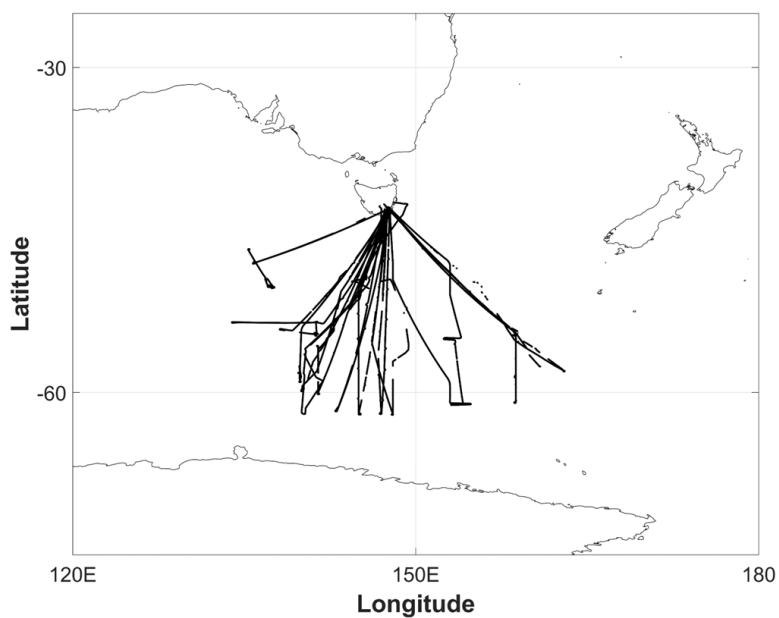
- Storelvmo, T.: Aerosol Effects on Climate via Mixed-Phase and Ice Clouds, *Annu. Rev. Earth Planet. Sci.*, 45, 199–222, <https://doi.org/10.1146/annurev-earth-060115-012240>, 2017.
- Tan, I. and Storelvmo, T.: Sensitivity Study on the Influence of Cloud Microphysical Parameters on Mixed-Phase Cloud Thermodynamic Phase Partitioning in CAM5, *J. Atmos. Sci.*, 73, 709–728, <https://doi.org/10.1175/JAS-D-15-0152.1>, 2016.
- 650 Tan, I., Storelvmo, T., and Zelinka, M. D.: Observational constraints on mixed-phase clouds imply higher climate sensitivity, *Science* (80-. ), 352, 224–227, <https://doi.org/10.1126/science.aad5300>, 2016.
- Wallace, J. M. and Hobbs, P. V.: *Atmospheric Science: An Introductory Survey*, New York, USA, <https://doi.org/10.1016/C2009-0-00034-8>, 1977.
- Wang, Z., and Coauthors: Single Aircraft Integration of Remote Sensing and In Situ Sampling for the Study of Cloud Microphysics and Dynamics. *Bull. Amer. Meteor. Soc.*, 93, 653–668, <https://doi.org/10.1175/BAMS-D-11-00044.1>, 2012.
- 655 Wang, Y., McFarquhar, G. M., Rauber, R. M., Zhao, C., Wu, W., Finlon, J. A., Stechman, D. M., Stith, J., Jensen, J. B., Schnaiter, M., Järvinen, E., Waitz, F., Vivekanandan, J., Dixon, M., Rainwater, B., and Toohey, D. W.: Microphysical Properties of Generating Cells Over the Southern Ocean: Results From SOCRATES, *J. Geophys. Res. Atmos.*, 125, 1–23, <https://doi.org/10.1029/2019JD032237>, 2020.
- 660 Westbrook, C. D. and Illingworth, A. J.: Evidence that ice forms primarily in supercooled liquid clouds at temperatures > 27°C, *Geophys. Res. Lett.*, 38, 1–4, <https://doi.org/10.1029/2011GL048021>, 2011.
- Wood, R., and Field, P. R.: The Distribution of Cloud Horizontal Sizes. *J. Climate*, 24, 4800–4816, <https://doi.org/10.1175/2011JCLI4056.1>, 2011.
- Wu, W., and McFarquhar, G. M.: On the impacts of different definitions of maximum dimension for nonspherical particles recorded by 2D imaging probes. *Journal of Atmospheric and Oceanic Technology*, 33(5), 1057–1072. <https://doi.org/10.1175/JTECH-D-15-0177.1>, 2016.
- Yang, C. A., Diao, M., Gettelman, A., Zhang, K., Sun, J., McFarquhar, G., and Wu, W.: Ice and Supercooled Liquid Water Distributions Over the Southern Ocean Based on In Situ Observations and Climate Model Simulations, *J. Geophys. Res. Atmos.*, 126, <https://doi.org/10.1029/2021JD036045>, 2021.
- 670 Yip, J., Diao, M., Silber, I., and Gettelman, A.: Evaluation of the CAM6 Climate Model Using Cloud Observations at McMurdo Station, Antarctica, *J. Geophys. Res.— Atmos.*, 126, 1–21, <https://doi.org/10.1029/2021JD034653>, 2021.
- Zaremba, T. J., Rauber, R. M., McFarquhar, G. M., Hayman, M., Finlon, J. A., and Stechman, D. M.: Phase Characterization of Cold Sector Southern Ocean Cloud Tops: Results From SOCRATES, *J. Geophys. Res. Atmos.*, 125, <https://doi.org/10.1029/2020JD033673>, 2020.
- 675 Zhang, M., Liu, X., Diao, M., D’Alessandro, J. J., Wang, Y., Wu, C., Zhang, D., Wang, Z., and Xie, S.: Impacts of Representing Heterogeneous Distribution of Cloud Liquid and Ice on Phase Partitioning of Arctic Mixed-Phase Clouds with NCAR CAM5, *J. Geophys. Res. Atmos.*, 124, 13071–13090, <https://doi.org/10.1029/2019JD030502>, 2019.
- Zhao, X. and Liu, X.: Global Importance of Secondary Ice Production, *Geophys. Res. Lett.*, 48, 1–11, <https://doi.org/10.1029/2021GL092581>, 2021.

680 Zhao, X., Liu, X., Burrows, S., DeMott, P. J., Diao, M., McFarquhar, G. M., et al. Important ice processes are missed by the  
Community Earth System Model in Southern Ocean mixed-phase clouds: Bridging SOCRATES observations to model  
developments. *Journal of Geophysical Research: Atmospheres*, 128, e2022JD037513. <https://doi.org/10.1029/2022JD037513>,  
2023.

685

**Table 1.** Definitions of four transition phases of mixed-phase clouds, alongside their required spatial ratios of LCR, ICR, and MCR.

Phase	Description	Number of seconds	Number of TCRs	Spatial Ratio of LCR	Spatial Ratio of ICR	Spatial Ratio of MCR
				M1 = length of LCR / total segment length	M2 = length of ICR / total segment length	M3 = length of MCR / total segment length
1	Only LCR	8243	1163	M1 = 1	M2 = 0	M3 = 0
2	MCR appears	12557 (LCR: 11096, MCR: 1461)	142	$0 < M1 < 1$	M2 = 0	$0 < M3 \leq 1$
3	Pure ICR must appear	11988 (LCR: 3478, MCR: 2973, ICR: 5537)	249	$0 \leq M1 < 1$	$0 < M2 < 1$	$0 \leq M3 < 1$
4	Only ICR	8646	1193	M1 = 0	M2 = 1	M3 = 0



690

**Figure 1.** Map of the flight tracks for SOCRATES for only temperatures between 0°C and -40°C.

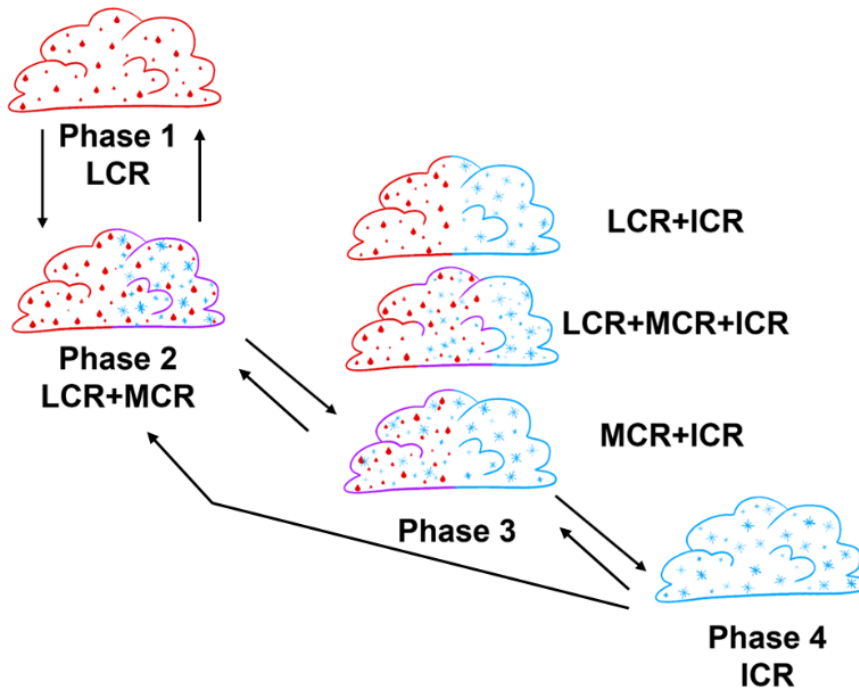
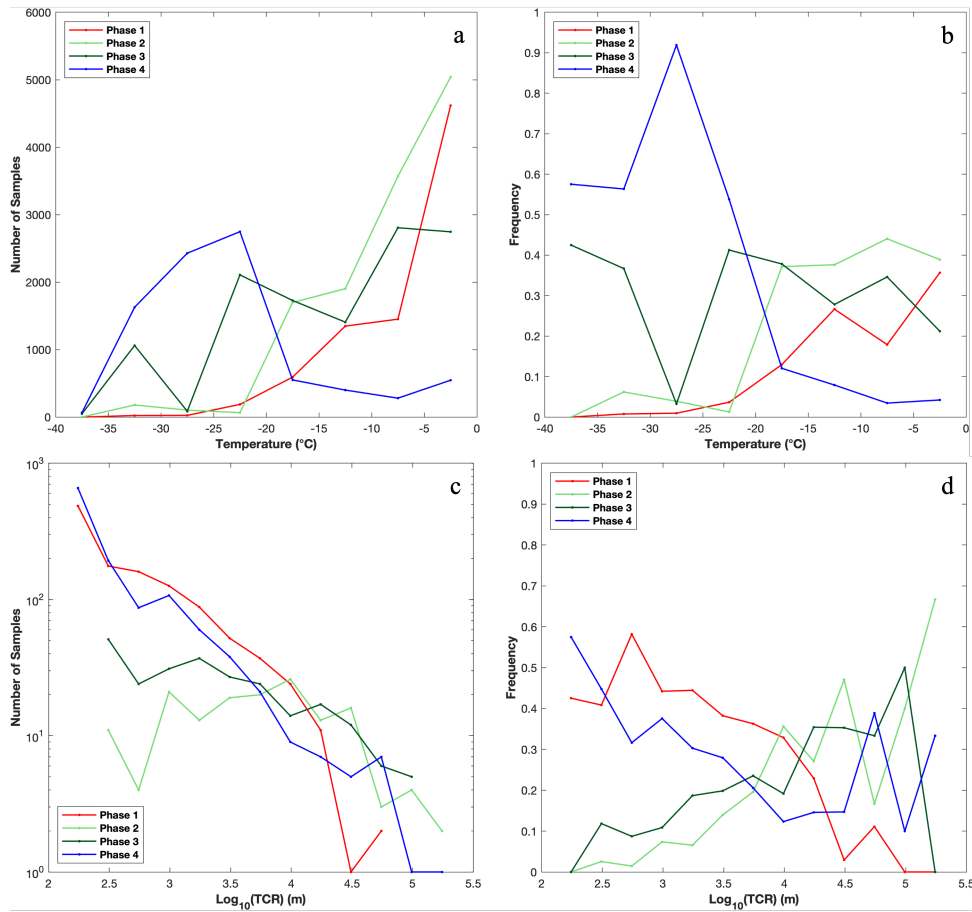


**Figure 2.** A conceptual diagram of the four transition phases for the phase exchange between supercooled liquid water and ice particles in mixed-phase clouds. Red, blue, and purple shading indicates liquid cloud region (LCR), ice cloud region (ICR) and mixed cloud region (MCR), respectively.

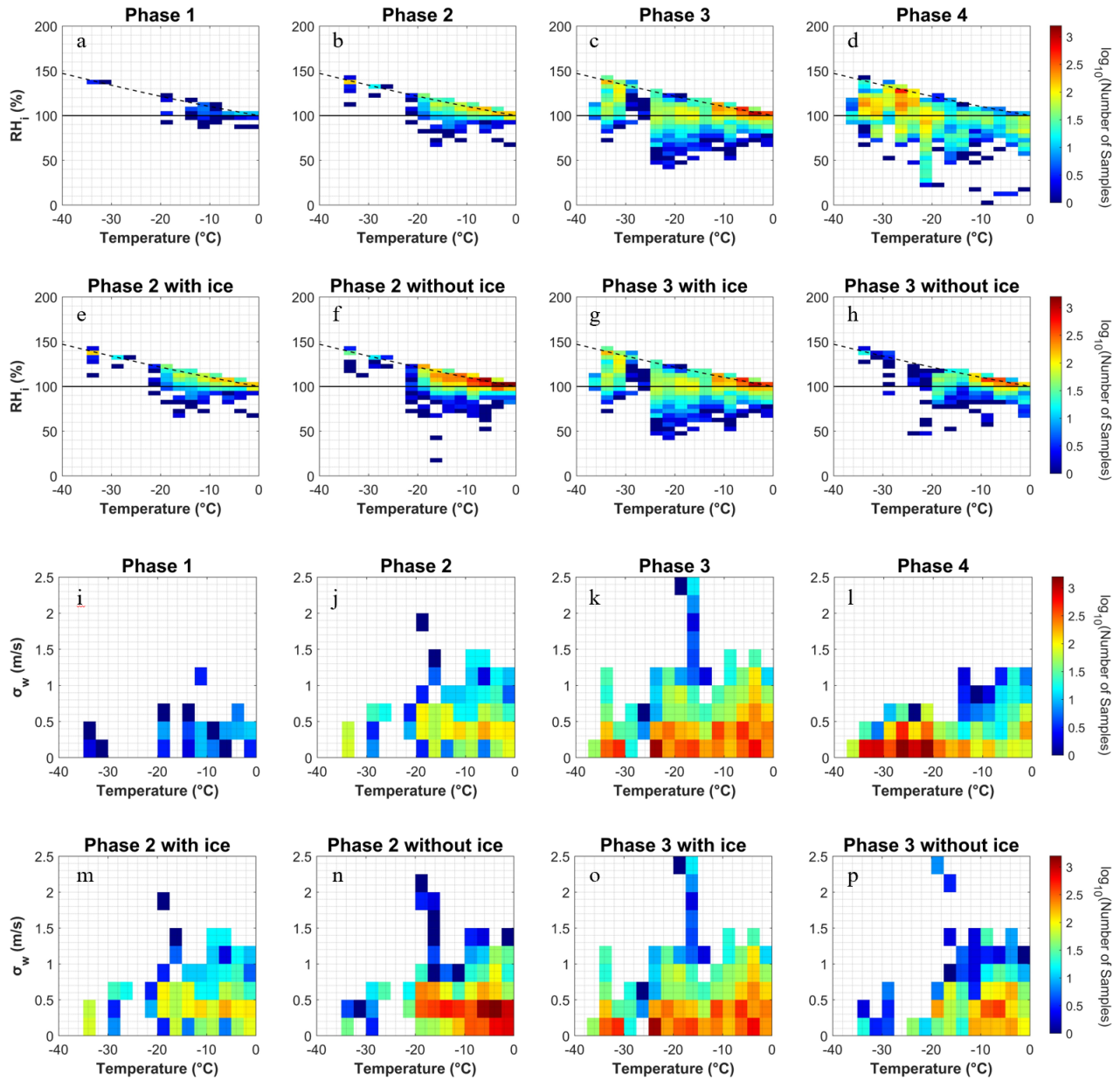




700

**Figure 3.** Distributions of four transition phases at various temperatures in terms of (a) number of 1-Hz samples and (b) frequency of each phase. In (b), the frequency of each phase is normalized by the number of samples of all phases in each 5-degree temperature bin. (c) Number of 1-Hz samples and (d) frequency distribution of TCR lengths in logarithmic scale. In (d), frequency is calculated as the number of 1-Hz samples of a specific phase divided by the total number of 1-Hz in-cloud samples in each  $10^{0.25}$  bin.

705



710 **Figure 4.** Distributions of (a-h)  $RH_i$  and (i-p)  $\sigma_w$  in various transition phases as a function of temperature. Dashed lines in (a) – (h) indicate liquid saturation.

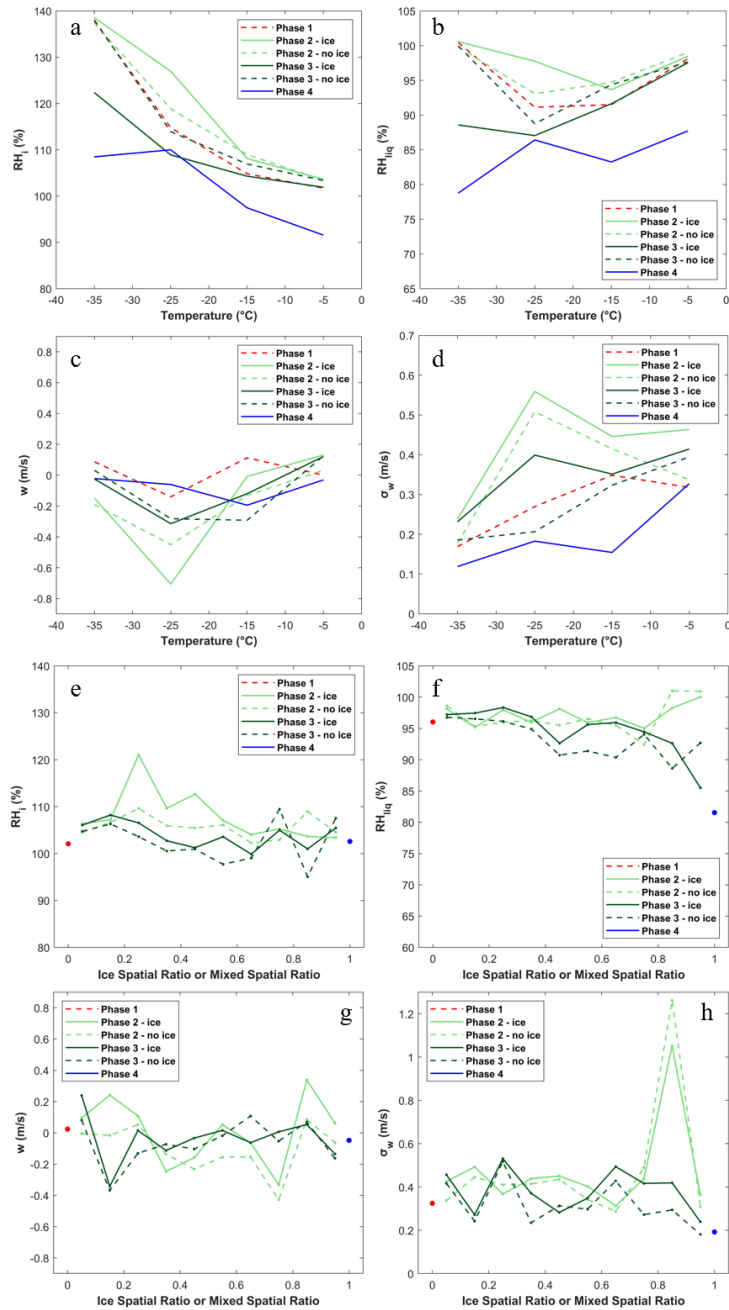
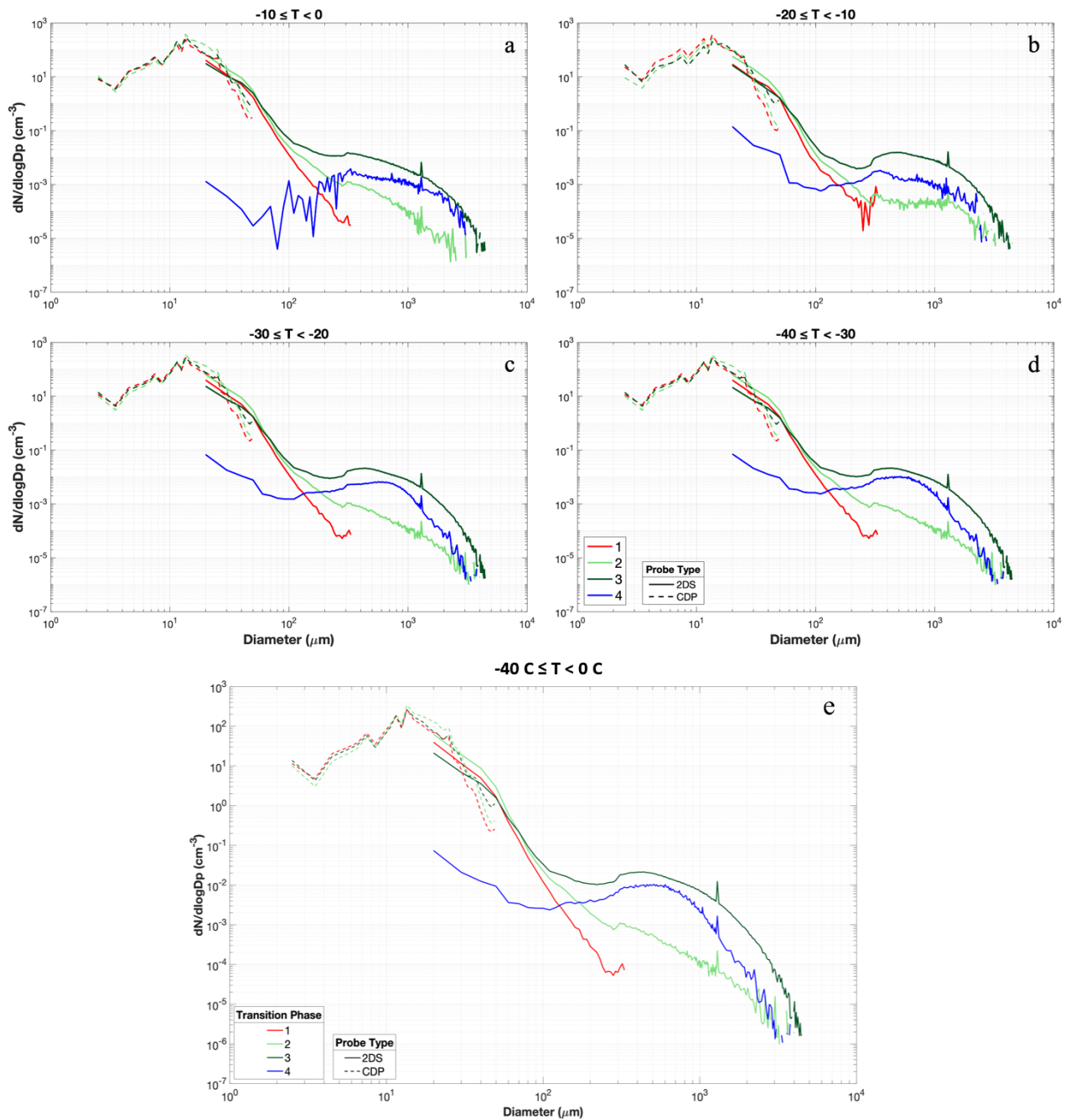
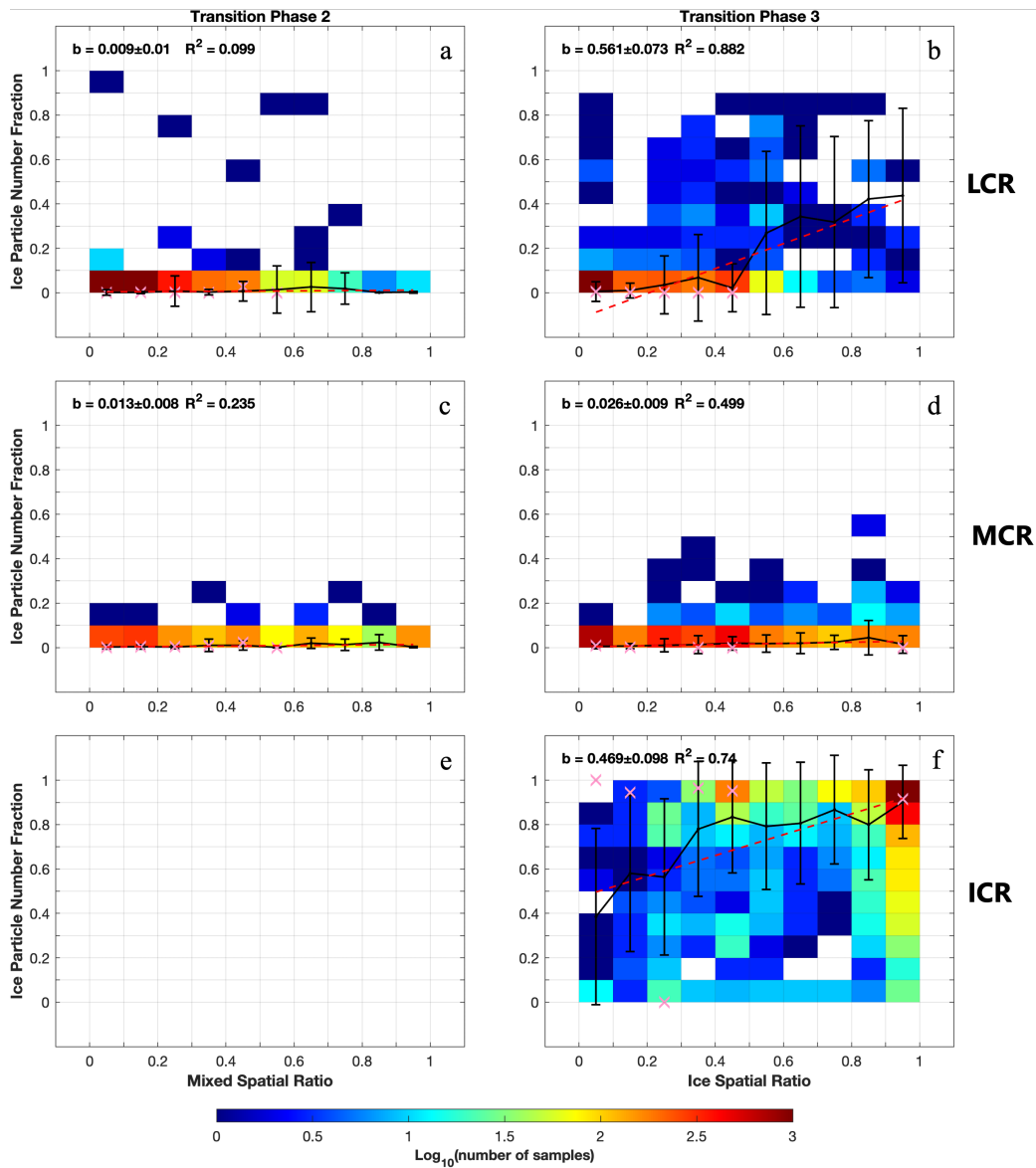


**Figure 5.** Distributions of (a)  $RH_i$ , (b)  $RH_{liq}$ , (c) vertical velocity ( $w$ ), and (d) standard deviation of vertical velocity ( $\sigma_w$ ) for various transition phases at different temperatures. (e-h) Similar to (a-d), but in relation to various mixed spatial ratios or ice spatial ratios. Phases 1 and 4 show ice spatial ratio at 0 and 1, respectively, and therefore only a single dot is shown for phases 1 and 4 in (e-h).



720 **Figure 6.** Particle size distribution of the four transition phases for mixed-phase clouds separated by probe types and temperature ranges. Phase 4 only shows 2DS measurements because ice particles measured by CDP are excluded from the analysis.



725 **Figure 7.** Relationship between ice particle number fraction and mixed spatial ratio or ice spatial ratio, separated by the  
 transition phases (phase 2 in column 1 and phase 3 in column 2), and by various cloud segments – (a, b) LCR, (c, d) MCR  
 and (e, f) ICR. Average values for each ice spatial ratio bin are shown in black solid lines, with vertical bars representing  
 standard deviations. Linear fit is shown in red dashed line. Average values of generating cells (time series obtained from  
 Wang et al. (2020)) are in pink “X” markers. The slope value  $b$ , its associated standard deviation, and the ordinary R-squared  
 730 value are shown in the legend.

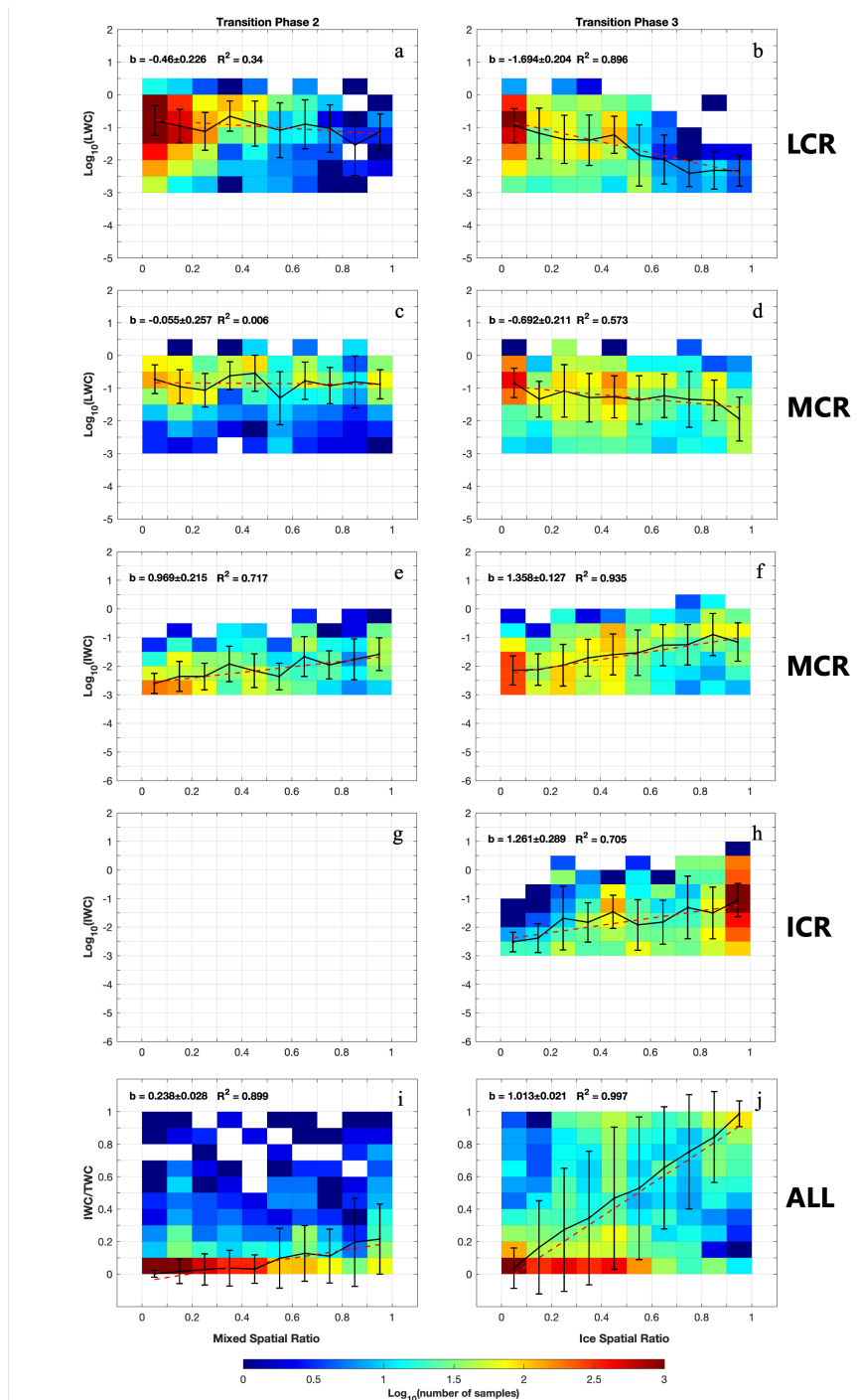


**Figure 8.** Similar to Figure 7, but showing (a-d) LWC ( $\text{g m}^{-3}$ ), (e-h) IWC ( $\text{g m}^{-3}$ ) and (i and j) ice mass fraction in relation to mixed spatial ratio for phase 2 and ice spatial ratio for phase 3, separated by the transition phases and cloud regions.

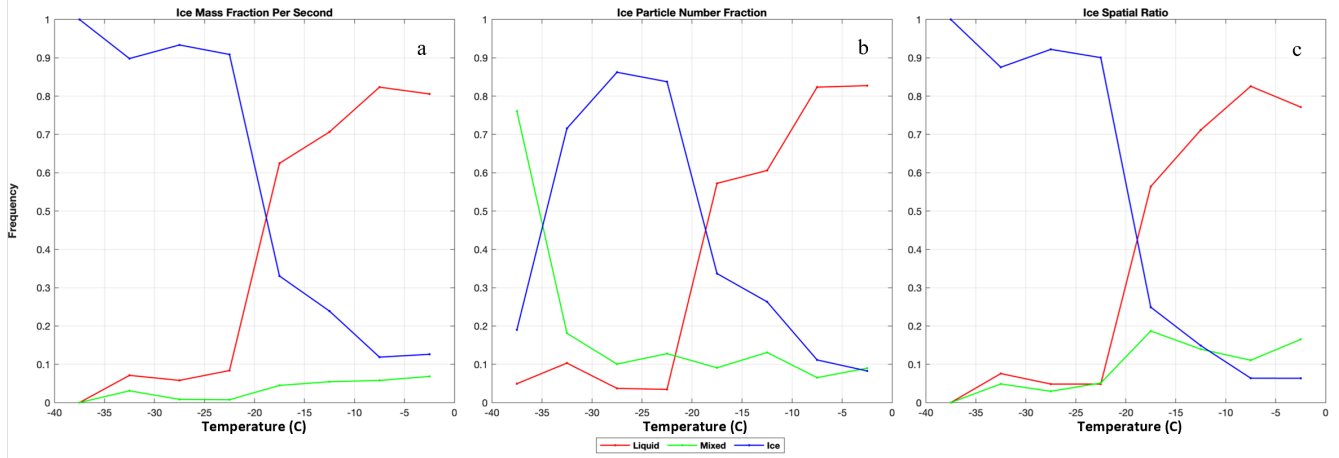
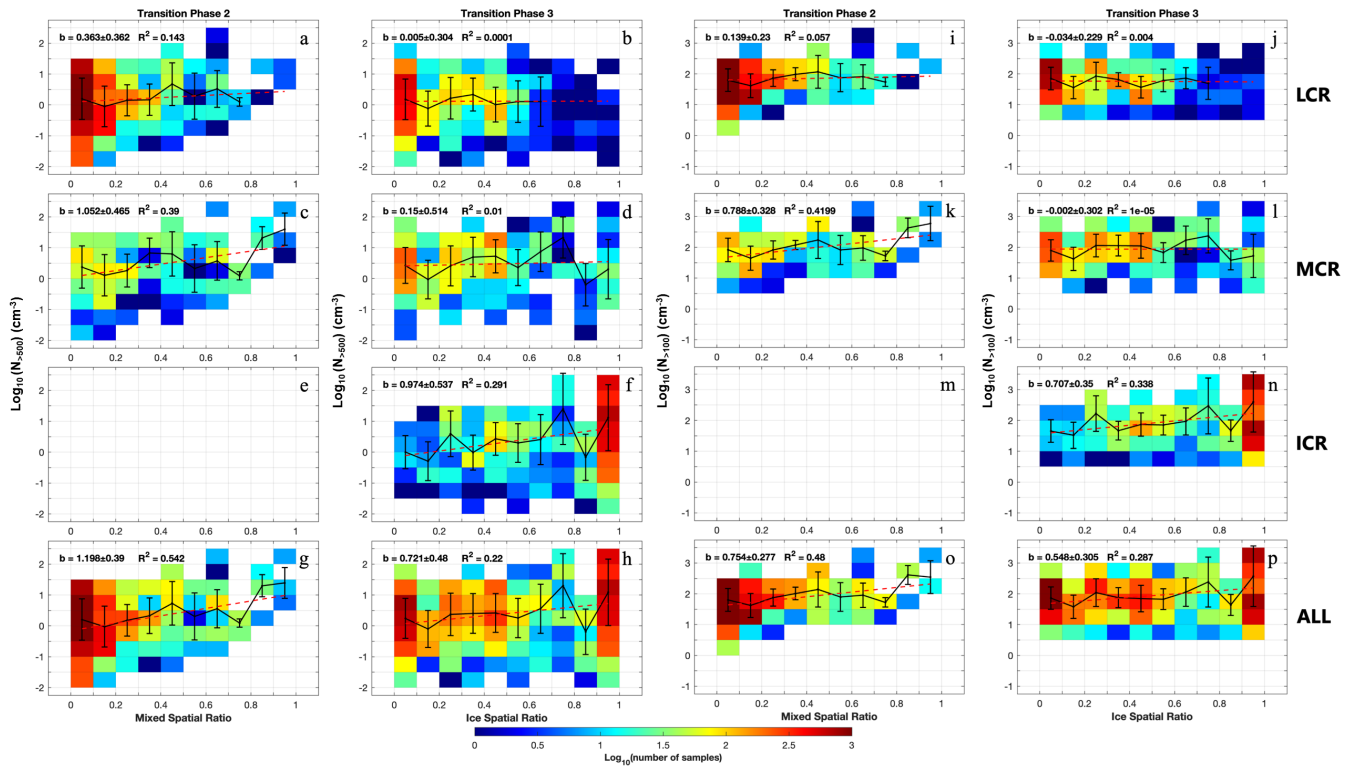


**Figure 9.** Cloud phase occurrence frequencies at various temperatures. Cloud phase identification methods are based on (a) ice mass fraction per second, (b) ice particle number fraction per second, and (c) ice spatial ratio calculated for individual consecutive TCR.



740

**Figure 10.** Similar to Figure 7, but showing logarithmic scale (a-h)  $N_{>500}$  and (i-p)  $N_{>100}$  in relation to mixed spatial ratio or ice spatial ratio, separated by the transition phases and cloud regions. The last row represents all cloud regions in a specific transition phase. The aerosol number concentrations represent the moving average values of every 50 seconds.